LUND UNIVERSITY

Monitoring techniques for embankment dams: A study on ERT and IP measurements, and seepage modelling of the Älvkarleby test dam
A multi-method approach to investigating internal anomalies in an embankment dam

Norooz, Reyhaneh

2025

Citation for published version (APA):
Norooz, R. (2025). *Monitoring techniques for embankment dams: A study on ERT and IP measurements, and seepage modelling of the Älvkarleby test dam: A multi-method approach to investigating internal anomalies in an embankment dam* . Department of Biomedical Engineering, Lund university.

Total number of authors:
1

Monitoring techniques for embankment dams

A study on ERT and IP measurements, and seepage modelling of the Älvkarleby test dam

REYHANEH NOROOZ

DIVISION OF ENGINEERING GEOLOGY | FACULTY OF ENGINEERING | LUND UNIVERSITY

Monitoring techniques for embankment dams: A study on ERT and IP measurements, and seepage modelling of the Älvkarleby test dam

Monitoring techniques for embankment dams: A study on ERT and IP measurements, and seepage modelling of the Älvkarleby test dam

A multi-method approach to investigating internal anomalies in an embankment dam

Reyhaneh Norooz

LUND UNIVERSITY

Organization: LUND UNIVERSITY

Document name: Doctoral dissertation

Date of issue 2025-10-06

Author(s): Reyhaneh Norooz

Sponsoring organization:

Title and subtitle: Monitoring techniques for embankment dams: A study on ERT and IP measurements, and seepage modelling of the Älvkarleby test dam - A multi-method approach to investigating internal anomalies in an embankment dam

Abstract:

Modern society depends on dams for renewable hydropower, water supply, and flood control. As climate change increases the frequency of extreme rainfall and flood events, and as the demand for renewable energy sources continues to grow, ensuring the safety of these critical structures becomes more urgent than ever. One of the most serious hidden threats in embankment dams is internal erosion – a slow process where fine particles are washed out from within the dam, potentially leading to leaks, sinkholes, or even failure. This process is difficult to detect using traditional visual inspections, which is why engineers are seeking innovative ways to monitor dam health.

The study is part of a Swedish research project exploring advanced geophysical techniques to detect internal erosion in embankment dams. The methods we tested are called Electrical Resistivity Tomography (ERT) and Induced Polarization (IP). These are non-invasive techniques that work like a kind of "medical scan" for dams. Electrodes placed in and around the structure measure how easily electric currents pass through the dam materials. By analysing both resistivity and chargeability (how materials temporarily store electric charge), we can generate 3D images of the dam's interior and gain insights into both moisture content and soil grain size—factors that are critical for assessing erosion and material integrity.

To test the effectiveness of ERT and IP in real-world conditions and compare them with other monitoring techniques, a 4 m high test embankment dam was constructed in Älvkarleby, Sweden. This dam contained six engineered defects (such as crushed rock zones and foreign material blocks) deliberately hidden within its core and filter zones. Their locations were unknown to the monitoring team, simulating the challenge of detecting unknown damage in an operational dam.

Between 7 500 and 14 000 ERT and IP data points were collected daily. These were processed using 3D inversion techniques to produce evolving models of resistivity and chargeability over time. The combined approach proved more powerful than either method alone.

The results were promising. Both ERT and IP successfully detected two of the five core defects – a horizontal and a vertical crushed-rock zone. A third defect, a concrete block in the core, was weakly indicated by ERT but with some positional error. One defect, a wooden block in the core, became visible only after three years of monitoring. The fifth core defect – a crushed-rock zone at the abutment – remained undetected, likely due to its small size and poor resolution in that specific area. This highlights a key challenge: resolution and electrode coverage are critical for successful detection, especially in full-scale applications. The fine filter defect was detected after two years of dam operation through both ERT and IP, appearing as a large anomalous zone with high resistivity and low chargeability.

In addition, the combined use of ERT and IP helped detect anomalous zones unrelated to the engineered defects. After the dam was dismantled, some of these anomalies were confirmed to be zones of internal erosion, further demonstrating the value of these methods.

Another important contribution of this research was the integration of geophysical data into seepage modelling. The ERT data significantly improved the characterization of dam materials and allowed for more precise delineation of water pathways. This, in turn, enhanced the accuracy of seepage models, leading to better predictions of potential leakage zones and critical weak points within the structure. By combining geophysical imaging with traditional seepage modelling, the study demonstrated how ERT can support more reliable dam safety evaluations.

Although not all defects were detected during the initial monitoring phase—and some only became apparent after several years—the results demonstrate that ERT, IP, and the integration of geophysical methods with seepage modelling are powerful tools for long-term dam monitoring and enhancing characterization of dam materials.

Key words: Electrical Resistivity Tomography, Induced Polarization, Seepage modelling, Embankment dam, Internal erosion, Monitoring techniques

Classification system and/or index terms (if any)

Supplementary bibliographical information

Language: English

ISSN and key title:

ISBN: 978-91-8104-671-7

Recipient's notes

Number of pages: 196

Price: Free

Security classification:

I, the undersigned, being the copyright owner of the abstract of the above-mentioned dissertation, hereby grant to all reference sources permission to publish and disseminate the abstract of the above-mentioned dissertation.

Signature

Date 2025-09-19

Monitoring techniques for embankment dams: A study on ERT and IP measurements, and seepage modelling of the Älvkarleby test dam

A multi-method approach to investigating internal anomalies in an embankment dam

Reyhaneh Norooz

LUND
UNIVERSITY

Acknowledgement

Reyhaneh Norooz

Lund, September 2025

Table of Contents

Popular science summary

Modern society depends on dams for renewable hydropower, water supply, and flood control. As climate change increases the frequency of extreme rainfall and flood events, and as the demand for renewable energy sources continues to grow, ensuring the safety of these critical structures becomes more urgent than ever. One of the most serious hidden threats in embankment dams is internal erosion – a slow process where fine particles are washed out from within the dam, potentially leading to leaks, sinkholes, or even failure. This process is difficult to detect using traditional visual inspections, which is why engineers are seeking innovative ways to monitor dam health.

The study is part of a Swedish research project exploring advanced geophysical techniques to detect internal erosion in embankment dams. The methods we tested are called Electrical Resistivity Tomography (ERT) and Induced Polarization (IP). These are non-invasive techniques that work like a kind of "medical scan" for dams. Electrodes placed in and around the structure measure how easily electric currents pass through the dam materials. By analysing both resistivity and chargeability (how materials temporarily store electric charge), we can generate 3D images of the dam's interior and gain insights into both moisture content and soil grain size— factors that are critical for assessing erosion and material integrity.

To test the effectiveness of ERT and IP in real-world conditions and compare them with other monitoring techniques, a 4 m high test embankment dam was constructed in Älvkarleby, Sweden. This dam contained six engineered defects (such as crushed rock zones and foreign material blocks) deliberately hidden within its core and filter zones. Their locations were unknown to the monitoring team, simulating the challenge of detecting unknown damage in an operational dam.

Between 7 500 and 14 000 ERT and IP data points were collected daily. These were processed using 3D inversion techniques to produce evolving models of resistivity and chargeability over time. The combined approach proved more powerful than either method alone.

The results were promising. Both ERT and IP successfully detected two of the five core defects – a horizontal and a vertical crushed-rock zone. A third defect, a concrete block in the core, was weakly indicated by ERT but with some positional error. One defect, a wooden block in the core, became visible only after three years of monitoring. The fifth core defect – a crushed-rock zone at the abutment – remained undetected, likely due to its small size and poor resolution in that specific area. This highlights a key challenge: resolution and electrode coverage are critical for successful detection, especially in full-scale applications. The fine filter defect

was detected after two years of dam operation through both ERT and IP, appearing as a large anomalous zone with high resistivity and low chargeability.

In addition, the combined use of ERT and IP helped detect anomalous zones unrelated to the engineered defects. After the dam was dismantled, some of these anomalies were confirmed to be zones of internal erosion, further demonstrating the value of these methods.

Another important contribution of this research was the integration of geophysical data into seepage modelling. The ERT data significantly improved the characterization of dam materials and allowed for more precise delineation of water pathways. This, in turn, enhanced the accuracy of seepage models, leading to better predictions of potential leakage zones and critical weak points within the structure. By combining geophysical imaging with traditional seepage modelling, the study demonstrated how ERT can support more reliable dam safety evaluations.

Although not all defects were detected during the initial monitoring phase—and some only became apparent after several years—the results demonstrate that ERT, IP, and the integration of geophysical methods with seepage modelling are powerful tools for long-term dam monitoring and enhancing characterization of dam materials.

Populärvetenskaplig sammanfattning

Det moderna samhället är beroende av dammar för förnybar vattenkraft, vattenförsörjning och översvämningskontroll. I takt med att klimatförändringarna ökar frekvensen av extrem nederbörd och översvämningar, och efterfrågan på förnybara energikällor fortsätter att växa, blir det allt viktigare att säkerställa säkerheten hos dessa kritiska strukturer. Ett av de allvarligaste och mest svårupptäckta hoten i fyllningsdammar är intern erosion – en långsam process där finpartiklar sköljs bort inuti dammen, vilket kan leda till läckage, sättningar eller till och med haveri. Denna process är svår att upptäcka med traditionella visuella inspektioner, vilket gör att ingenjörer söker nya innovativa metoder för att övervaka dammars hälsa.

Arbetet är en del av ett svenskt forskningsprojekt där avancerade geofysiska tekniker har undersökts för att upptäcka intern erosion i fyllningsdammar. De metoder vi testat kallas Elektrisk Resistivitetstomografi (ERT) och Inducerad Polarisation (IP). Dessa är icke-invasiva tekniker som fungerar som en slags "medicinsk skanning" av dammar. Elektroder placeras i och runt dammen för att mäta hur lätt elektrisk ström passerar genom dammstrukturen. Genom att analysera både resistivitet och laddningsförmåga (hur material tillfälligt lagrar elektrisk laddning) kan vi skapa tredimensionella bilder av dammens inre och få insikter om både fuktinnehåll och kornstorlek – faktorer som är avgörande för att bedöma erosion och materialens tillstånd.

För att testa ERT och IP i verkliga förhållanden och jämföra dem med andra övervakningstekniker byggdes en 4 meter hög testdamm i Älvkarleby, Sverige. Dammen innehöll sex medvetet inbyggda men dolda defekter – såsom zoner med krossad sten och inlagda främmande materialblock – som simulerade skador som kan byggas in eller uppstå naturligt över tid. Dessa defekters placering var okänd för övervakningsteamet, vilket skapade realistiska förhållanden för att testa teknikerna.

Mellan 7 500 och 14 000 mätpunkter med ERT och IP registrerades dagligen och bearbetades med tredimensionella inversionsmetoder för att skapa modeller av resistivitet och laddningsförmåga över tid. Den kombinerade metoden visade sig vara kraftfullare än var och en av teknikerna för sig.

Resultaten är lovande. Både ERT och IP lyckades initialt identifiera två av de fem defekterna i dammens kärna – en horisontell och en vertikal zon med krossad sten. En tredje defekt, ett betongblock i kärnan, kunde svagt urskiljas av ERT-metoden, dock med viss positionsfel. En fjärde defekt, ett träblock i kärnan, blev synlig först efter tre års övervakning. Den femte defekten – en krossad sten-zon vid dammens anslutning mot berg (abutment) – förblev oupptäckt, sannolikt på grund av dess lilla storlek och den låga dataupplösningen i området. Detta understryker en viktig utmaning: god täckning med elektroder och hög upplösning är avgörande för att

upptäcka defekter, särskilt i fullskalig tillämpning. Defekten i det fina filtret identifierades efter två års drift, då den visade sig som en stor anomali med hög resistivitet och låg laddningsförmåga.

Dessutom hjälpte den kombinerade användningen av ERT och IP till att identifiera anomalier som inte var relaterade till de avsiktliga defekterna. När dammen demonterades kunde flera av dessa zoner bekräftas vara områden med intern erosion, vilket ytterligare visar värdet av dessa metoder.

En annan viktig insats i detta arbete var integrationen av geofysiska data i modeller för genomströmning (läckage). ERT-data förbättrade materialkarakteriseringen av dammen avsevärt och gjorde det möjligt att mer noggrant avgränsa flödesvägar. Detta ledde till förbättrade genomströmningsmodeller och mer tillförlitliga förutsägelser av potentiella läckagezoner och svaga punkter i dammen. Genom att kombinera geofysisk avbildning med traditionell hydraulisk modellering visade studien hur ERT kan stödja mer tillförlitliga säkerhetsbedömningar av dammar.

Trots att inte alla defekter kunde upptäckas under den inledande övervakningsperioden – och vissa först blev synliga efter flera år – visar resultaten att ERT, IP och kombinationen med genomströmningsmodellering är kraftfulla verktyg för långsiktig övervakning av dammar och för förbättrad karakterisering av dammarnas material.

List of Papers

Paper I

Norooz, R., Olsson, P.-I., Dahlin, T., Günther, T., & Bernstone, C. (2021). A geoelectrical pre-study of Älvkarleby test embankment dam: 3D forward modelling and effects of structural constraints on the 3D inversion model of zoned embankment dams. Journal of Applied Geophysics, 191, 104355. https://doi.org/10.1016/j.jappgeo.2021.104355

Paper II

Norooz, R., Nivorlis, A., Olsson, P.-I., Günther, T., Bernstone, C., & Dahlin, T. (2024). Monitoring of Älvkarleby test embankment dam using 3D electrical resistivity tomography for detection of internal defects. Journal of Civil Structural Health Monitoring, 14, 1275–1294. https://doi.org/10.1007/s13349-024-00785-x

Paper III

Norooz, R., Dahlin, T., & Toromanovic, J. (2025). Integration of seepage modelling and electrical resistivity monitoring data for the Älvkarleby test embankment dam, Sweden. Engineering Geology, 357, 108311. https://doi.org/10.1016/j.enggeo.2025.108311

Paper IV

Norooz, R., Dahlin, T., & Johansson S. (2025). 3D DCIP for detection of internal defects in Älvkarleby test embankment dam. Manuscript for submission to Geophysical Journal International

Author's contribution to the papers

Paper I

The concept of 3D inversion modelling, as well as the design of the electrode layout and measurement configurations, was proposed by the supervisor and one of the co-authors. The thesis author contributed by introducing the use of constraints in the inversion modelling and was responsible for developing the methodology and implementing the numerical modelling, including 3D synthetic ERT forward modelling, inversion of the synthetic data, and the subsequent visualizations. As the lead author, she prepared the initial manuscript draft, incorporated feedback from co-authors and reviewers, and led the revision process through to the final version.

Paper II

The concept of 3D inversion modelling, the design of the electrode layout and measurement configurations, was proposed by the supervisor. The thesis author was responsible for developing the methodology, programming, and implementing the 3D ERT time-lapse inversion of the field data collected at the Älvkarleby test dam, as well as visualizing the resulting resistivity models. As the main author, she drafted the original manuscript, incorporated feedback from co-authors and reviewers, and led the submission and revision processes. The thesis author was not involved in the ERT data acquisition or the development of the data collection automation system, which was carried out by another co-author.

Paper III

The conceptualization and methodology of this study were developed by the thesis author. She was also responsible for data curation and visualization. As the main author, she drafted the original manuscript, incorporated feedback from co-authors and reviewers, and led the submission and revision processes. However, the author was not involved in the collection of ERT, pore pressure, turbidity, or leaked water rate data, which was carried out by other co-authors.

Paper IV

The supervisor introduced the concept of 3D inversion modelling and designed the electrode layout and measurement configurations. The thesis author was responsible for developing the methodology, programming, and implementing the single-time 3D ERT and IP inversion of the field data collected at the Älvkarleby test dam, as well as processing and visualizing the resistivity and chargeability models. She also prepared the initial manuscript draft, incorporated feedback from co-authors and reviewers, and managed the submission and revision process. The author was not involved in the acquisition of the ERT and IP data.

Abbreviations

ICODS	Interagency Committee on Dam Safety
ERT	Electrical Resistivity Tomography
IP	Induced Polarization
3D	three-dimensional
FE	finite element
ICOLD	International Commission on Large Dams
CLE	concentrated leak erosion
BEP	backward erosion piping
II	internal instability
CE	contact erosion
DTS	distributed fibre optic temperature sensing
2D	two-dimensional
DC	direct current
EDL	electrical double layer
TDIP	time-domain IP
AC	alternating current
FDIP	frequency-domain IP
pyGIMLi	Python Geophysical Inversion and Modelling Library
pyBERT	Python Boundless Electrical Resistivity Tomography
4D	four-dimensional
IIR	Infinite Impulse Response
FEM	Finite Element Method
FDM	Finite Difference Method
BEM	Boundary Element Method
VRD	Vattenfall R&D
PSD	particle size distribution
LTU	Luleå University of Technology

1 Introduction

Hydropower embankment dams play a crucial role in sustainable energy production, and in many countries there are limited opportunities for constructing new hydropower plants. The continued operation and safety of existing embankment dams are therefore of paramount importance. One of the most critical threats to the integrity of embankment dams is internal erosion, which can develop unnoticed within the dam structure and ultimately lead to failure if not detected in time (Interagency Committee on Dam Safety (ICODS), 2015).

Conventional methods for detecting internal erosion, such as leakage monitoring and visual inspections, often identify damage only at a late stage, when significant material loss has already occurred (Jung et al., 2015). Therefore, the development of advanced monitoring techniques is essential to enhance dam safety and enable early detection of weak zones.

Electrical Resistivity Tomography (ERT) is a geophysical method that has shown potential for detecting internal erosion by measuring spatial and temporal variations in electrical resistivity (Binley & Slater, 2020). The method relies on differences in resistivity caused by factors such as water content, temperature variations, and soil composition. In the context of embankment dams, internal erosion processes can alter these factors, resulting in detectable changes in resistivity (Norooz et al., 2021). This makes ERT a promising tool for continuous monitoring of such structures.

Induced Polarisation (IP) is a geophysical method closely related to ERT but provides additional information about the subsurface by measuring the delayed response of materials to an applied electrical field (Marshall & Madden, 1959). This delay, known as chargeability, can help distinguish between different soil and material types, particularly when assessing fine-grained sediments or detecting changes in pore fluid composition. In the context of embankment dam monitoring, IP can be used to enhance the interpretation of ERT data by providing insights into the electrochemical properties of the dam materials. When combined with ERT, IP improves the identification of zones affected by internal erosion, as it helps differentiate between variations caused by water content changes.

A test embankment dam was constructed in Älvkarleby, Sweden, to evaluate the effectiveness of various monitoring techniques, including ERT and IP surveys. Designed to replicate a typical Swedish embankment dam, the structure was deliberately built with artificial defects to assess how well different methods could

detect them. The study was conducted as a blind test, meaning the monitoring teams were unaware of the defect locations, ensuring realistic and unbiased evaluation conditions. The dam was injected after two years to assess the extent to which the defects could be remediated. Magnetite was used in the injection material for some of the boreholes to make it detectable by the geophysical methods.

In addition to ERT and IP data analysis, a three-dimensional (3D) seepage model was developed for the Älvkarley test dam to gain a more comprehensive understanding of the dam's performance. Finite element (FE) seepage models are useful tools in geotechnical engineering, as they can theoretically model a wide range of problems. They are capable of accurately calculating flow velocity, flow paths, hydraulic gradients, and water head values, offering a detailed understanding of the behaviour of water within the dam (Nikrou & Pirboudaghi, 2024).

This thesis examines the applicability of the ERT method for detecting internal defects in embankment dams. It focuses on the method's detection capabilities, limitations, and practical implementation as a monitoring tool. By incorporating IP measurements, the study also investigates how combined geoelectrical techniques can improve the identification of seepage-related anomalies. Additionally, the integration of seepage modelling with ERT data will be assessed to determine how ERT can enhance the accuracy and effectiveness of seepage models. The results contribute to a broader understanding of how geoelectrical methods can be integrated into dam safety programs, offering insights into both the potential and the challenges of using ERT and IP for long-term embankment dam monitoring.

1.1   Background

The safety and long-term performance of embankment dams have become a growing concern as many existing structures continue to age. These dams are subjected to various environmental and operational stresses, including fluctuating water levels, seasonal temperature changes, and prolonged material degradation. Over time, these factors can contribute to internal erosion, a hidden yet severe process that gradually weakens the dam's structural integrity and increases the risk of failure. Addressing this issue requires a comprehensive understanding of how internal erosion develops and progresses within embankment dams.

Traditional dam monitoring techniques primarily rely on visual inspections and leakage measurements. While these methods are useful for detecting surface-level changes, they are often insufficient for identifying early-stage internal erosion, which occurs deep within the dam structure. By the time visible signs appear, such as increased seepage or material displacement, significant damage may have already taken place. This challenge underscores the necessity of developing more advanced and reliable monitoring technologies.

In recent years, geophysical methods have emerged as promising tools for assessing subsurface conditions in embankment dams. Among these, ERT offers the ability to detect internal changes by measuring electrical resistivity variations (Guo et al., 2022; Hojat et al., 2021; Khalil et al., 2024; Lee et al., 2020; Martínez-Moreno et al., 2018; Masi et al., 2020; Shin et al., 2019; Sjödahl et al., 2010; Wei et al., 2024). To enhance interpretation, ERT is often complemented by other approaches, such as IP (Abdulsamad et al., 2019), which provides additional insights into electrochemical properties and moisture conditions. These methods provide spatially continuous information, which is difficult to obtain using traditional techniques.

Despite these developments, several gaps remain in the literature. Most previous studies have applied ERT and/or IP, relied on short-term measurements, or investigated natural dams with unknown internal conditions, limiting the ability to directly validate geophysical measurements against actual internal erosion processes. In addition, the full 3D geometry and internal zonation of embankment dams are often simplified or neglected in inversion, reducing the realism and interpretability of results. To date, no study has fully combined long-term 3D ERT and IP monitoring and 3D inversion while accounting for material boundaries in a large-scale embankment dam.

The reliable estimation of material properties within dam bodies remains a major challenge for seepage modelling, despite extensive use of FE models in dam engineering, including back analysis, probabilistic modelling, coupled flow–deformation analysis, and AI-supported parameter estimation (e.g., Zheng et al., 2024; Bayat et al., 2019 and Chi et al., 2023). Accurately capturing the spatial heterogeneity of these properties is essential for trustworthy simulations and assessing internal erosion risks.

Although laboratory and field measurements provide valuable information, uncertainties remain regarding the spatial distribution of material properties throughout the dam body, particularly for different zones such as the core and filter. ERT offers a continuous, detailed view of internal material characteristics, and when combined with advanced 3D inversion techniques—including survey design, geometric factor calculations, and inversion meshes that respect material boundaries—it provides insights that have not been reported in previous studies.

Addressing these gaps, the present thesis integrates 3D ERT with 3D seepage modelling and incorporates 3D IP measurements alongside the ERT data. The study further evaluates the potential of ERT as a long-term monitoring method, providing new insights into internal erosion processes and material heterogeneity in embankment dams.

1.2 Aim and Objectives

Building on the research gaps identified above, the aim of this research is to investigate the applicability and effectiveness of ERT and IP for detecting internal erosion in embankment dams. Additionally, the study explores how integrating geophysical monitoring techniques with seepage modelling can enhance the definition of material properties in the dam body and improve the accuracy of these models.

To achieve this aim, the following objectives have been defined:
   i.   Evaluate the capability of ERT in detecting internal erosion – Assess how variations in electrical resistivity can be used to identify seepage paths and weak zones within embankment dams.
   ii.   Examine the role of IP in complementing ERT data – Investigate how chargeability measurements can enhance the interpretation of resistivity anomalies and improve the identification of erosion-prone areas.
   iii. Develop and validate a 3D seepage model – Use ERT data to guide the construction of a numerical model that simulates water flow within embankment dams.

By addressing these objectives, this research aims to contribute to the development of more reliable and proactive dam monitoring strategies, ultimately enhancing the safety and sustainability of embankment dams.

1.3 Limitations

While this research offers valuable insights into the applicability of ERT and IP for detecting internal erosion in embankment dams and the integration of seepage modelling guided by ERT results, several limitations must be acknowledged. These include methodological constraints, challenges in data interpretation, and practical considerations for implementation.
   i.   Methodological constraints: One of the primary limitations of this study is the controlled nature of the test environment. The test embankment dam in Älvkarleby was constructed with predefined defects to assess the effectiveness of geophysical monitoring techniques. While this setup allows for a systematic evaluation of ERT and IP, it does not fully replicate the complexity and variability found in real-world embankment dams. Factors such as unknown underground material, heterogeneous soil composition, natural aging processes, and varying hydrological conditions could influence the applicability of the methods in operational dams. Additionally, the spatial and temporal resolution of ERT and IP measurements may affect the detection accuracy. The electrode spacing and survey frequency were optimized for the test setup, but in larger,

operational dams, achieving a similar resolution may be challenging due to logistical constraints, such as electrode placement, accessibility, and long-term data collection feasibility.

ii. Data interpretation challenges: The interpretation of ERT and IP data is inherently complex and requires careful consideration of multiple influencing factors. Electrical resistivity variations can be affected by temperature fluctuations, mineralogical differences, and changes in water chemistry, which may lead to false positives or ambiguous results. While combining IP with ERT enhances data interpretation, distinguishing between different causes of resistivity anomalies remains a challenge. Moreover, the seepage model, although useful for understanding flow patterns and high-risk zones, is based on several assumptions regarding material properties and boundary conditions. The accuracy of model predictions depends on the reliability of input parameters derived from geophysical data. Any discrepancies between assumed and actual material properties can introduce uncertainties in the model outputs.

iii. Practical implementation considerations: While the study demonstrates the potential of integrating ERT and IP into dam monitoring programs, the practical implementation of these methods in full-scale embankment dams presents several challenges. Continuous monitoring requires the installation of buried electrodes, drilling to install them, and maintenance of electrode arrays, which may be difficult in dams with restricted access or regulatory limitations and may pose risks to dam integrity.

Despite these limitations, the findings of this research contribute to the advancement of geophysical monitoring techniques for embankment dam safety. Future studies should focus on refining data interpretation methods, improving long-term monitoring strategies, and addressing practical challenges associated with large-scale implementation.

2 Embankment dams

Embankment dams are among the most widely used dam types due to their adaptability to various foundation conditions and the availability of construction materials (Penman, 1986). These dams are constructed using natural materials, typically sourced locally. These materials are selected and placed in defined zones within the dam body to optimize their engineering properties. The construction process involves compacting these natural fills without the addition of binding agents, using heavy machinery (Novak et al., 2014). For long-term stability and safety, it is essential that the dam's design, construction and operation are carried out with high precision and care, as poor execution can lead to serious issues such as internal erosion in the future.

Internal erosion poses a significant threat to the structural integrity of embankment dams and the safety of downstream populations. It refers to the process by which water seeping through or beneath a dam gradually removes soil particles from within the dam body or its foundation (Figure 1). Over time, this particle transport can create voids, channels, or "pipes" that weaken the structure from within, potentially leading to sudden and catastrophic failure. The erosion is often undetectable until advanced stages, making early identification and intervention critical.
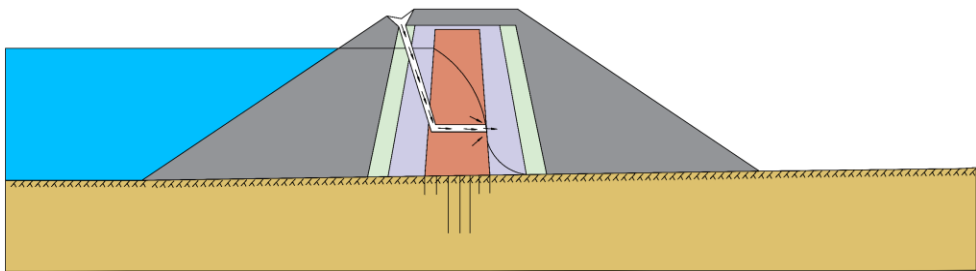

Figure 1. Separation and movement of particles in internal erosion (adopted from Sjödahl (2006)).

A study by Foster et al. (1998) at the University of New South Wales found that internal erosion accounted for approximately 54% of embankment dam failures worldwide since 1950. In response to the widespread occurrence of this failure

mode, a variety of monitoring methods have been developed and implemented to monitor seepage, assess risk, and apply appropriate mitigation measures.

This chapter provides an overview of the main types of embankment dams, the zoning principles used in their design, the issue of internal erosion, and the various monitoring techniques employed to ensure their long-term safety and performance.

2.1   Types of embankment dams

Embankment dams are broadly categorized into earthfill and rockfill types (Novak et al., 2014). However, this classification is not rigid, many dams incorporate both soil and rockfill materials in separate internal zones. While some smaller dams may use a homogeneous cross-section, most embankments feature an impermeable core (often of clay) supported by more permeable shoulder zones (Figure 2).

The impermeable core is a central element of an embankment dam, designed to prevent or significantly reduce the seepage of water through the dam structure (EL-Molla & Kilit, 2025) (Figure 2). Its primary function is to act as a barrier to water flow, thereby maintaining the hydraulic integrity and safety of the dam (Adamo et al., 2020). The core is typically constructed from low-permeability materials such as clay or other fine-grained soils, carefully compacted to ensure effectiveness.

Depending on the design and structural requirements, the core may be positioned centrally, slightly upstream of the centre, or along the upstream face—particularly in certain rock-fill dams (see Figure 3 c, e, f and Figure 4 a, b).

The core is usually supported by more permeable materials, support fill and filters, which provide structural stability and help manage pore water pressures (Figure 2). Filter zones play a crucial role in the stability and safety of embankment dams by controlling seepage and preventing internal erosion. They are typically divided into two main categories: fine filters and coarse filters (also referred to as gravel or transition filters), each serving distinct but complementary purposes.

Fine filters are placed directly adjacent to the impermeable core. Their primary function is to retain the fine particles of the core material while allowing water to pass through (International Commission On Large Dams (ICOLD), 1994). This helps prevent the migration of core material into surrounding zones, which could otherwise lead to internal erosion. Fine filters are designed according to specific grain size criteria to ensure compatibility with the core material, following well-established filter design rules (Figure 2).

Coarse filters, or gravel filters, are positioned outside the fine filter zones. Their main function is to serve as a transition between the fine filter and the coarser outer support fill materials. Coarse filters facilitate the safe dissipation of seepage water and provide drainage while continuing to prevent the movement of finer particles toward the downstream support fill (ICOLD, 1994). Like fine filters, they are

designed to meet gradation requirements to ensure proper filtration and permeability (Figure 2).

The supporting fill, commonly referred to as the shell, forms the outer zones of an embankment dam and provides structural stability, protection, and support to the inner core and filter zones (ICOLD, 1994). These zones are typically composed of coarse-grained materials such as gravel, crushed rock, or well-graded soil, selected for their strength, durability, and permeability (Figure 2).

One of the primary functions of the supporting fill is to resist the hydraulic and mechanical forces acting on the dam, including the weight of the water, seismic loads, and settlement of the structure (US Bureau of Reclamation, 2012). The upstream supporting fill provides support to the impermeable core and helps protect against wave action and erosion, often incorporating slope protection measures such as riprap. The downstream supporting fill facilitates the safe discharge of seepage water that passes through the core and filter systems, ensuring the stability of the dam under both steady-state and transient flow conditions (US Bureau of Reclamation, 2012).

In zoned embankment dams, the supporting fill is designed to work in combination with the core and filters, ensuring that each material zone performs its specific function without compromising the dam's overall integrity. Proper compaction, material selection, and geometric design are essential to prevent settlement, cracking, or differential movement that could endanger the impermeable core or create seepage paths.
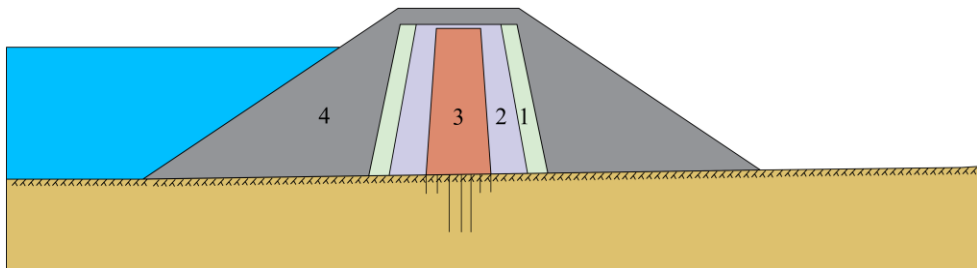
Figure 2. Cross-section of a zoned embankment dam with a central core, illustrating the principle zones. Core (3), fine and coarse filters (1, 2) and support fill (4).

The type of embankment dam selected depends largely on the availability and characteristics of local materials (Novak et al., 2014). In earthfill dams, over 50% of the structure consists of compacted soil, placed in thin layers under controlled moisture conditions (Novak et al., 2014). Figure 3 shows cross-sectional examples of several common types of earthfill embankments. Rockfill dams, in contrast, are characterized by a majority of coarse, frictional materials, and typically incorporate a discrete impermeable zone, either a central earth core or a thin concrete/asphalt membrane (Figure 4). In modern construction, the rockfill is carefully graded and

compacted in relatively thin layers using heavy machinery. As a result, the construction process is quite similar to that of an earthfill embankment (Novak et al., 2014).
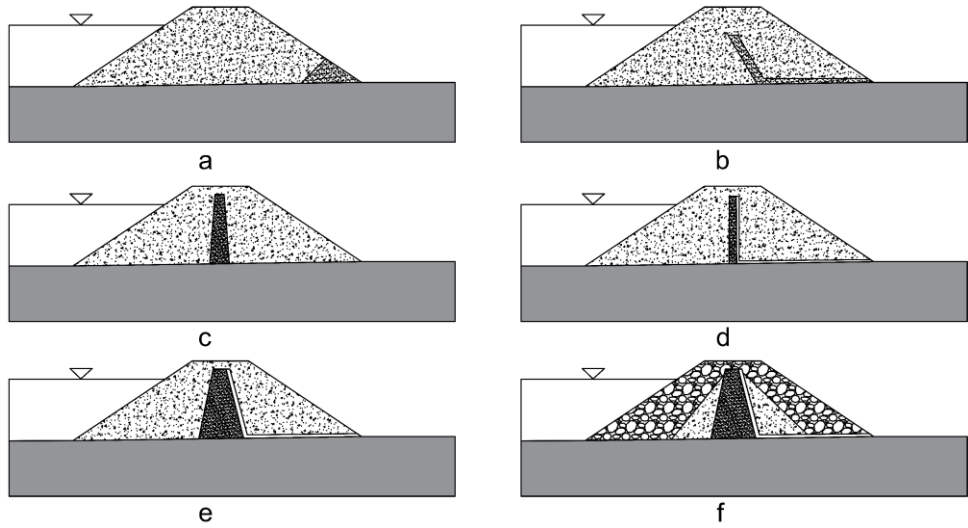
Figure 3. Main types of earthfill and earthfill–rockfill embankment dams: (a) Homogeneous dam with toe drain, (b) Homogeneous dam with chimney drain, (c) Earthfill dam with slender central clay core, (d) Earthfill dam with concrete core, (e) Earthfill dam with wide clay core, (f) Zoned earthfill/rockfill dam with central rolled clay core, including transition zones and drainage elements (adopted from Novak et al. (2014)).
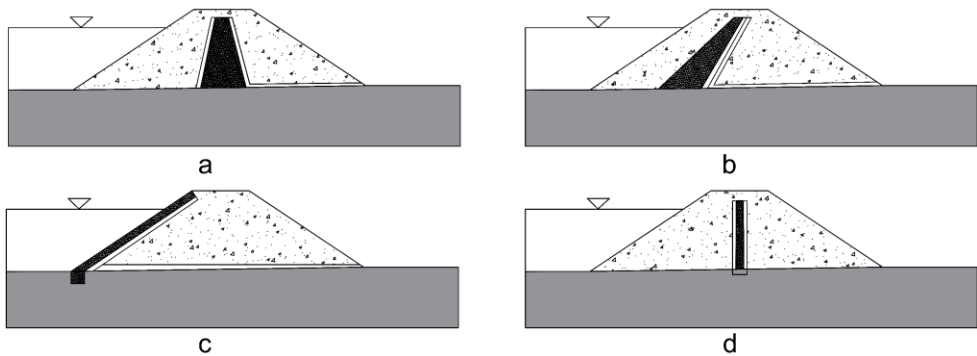
Figure 4. Main types of rockfill embankment dams: (a) Rockfill dam with central clay core, (b) Rockfill dam with inclined clay core, (c) Rockfill dam with concrete or asphaltic face, (d) Rockfill dam with central asphaltic membrane (adopted from Novak et al. (2014)).

2.2 Embankment dam failures

Foster et al. (1998, 2000), drawing on data from ICOLD archives (ICOLD, 1973, 1983, 1995), conducted a comprehensive statistical analysis of large dam failures constructed between 1800 and 1986. Their findings indicate that internal erosion accounts for approximately 50% of known failure cases in embankment dams, making it as prevalent a failure mode as overtopping caused by insufficient spillway capacity or malfunctioning outlet works (Figure 5). Internal erosion typically initiates at localized weak points within the dam body, where water can concentrate and gradually transport fine particles. These weak points often result from uneven compaction during construction, inhomogeneous material layers, or improperly designed transitions between the impervious core and surrounding filter and supporting fill zones. Over time, natural settlement, cracking, or biological activity (e.g., root channels or burrowing animals) can further exacerbate these vulnerabilities, ultimately undermining the dam's stability.

Spillway failure due to insufficient capacity is a leading cause, accounting for approximately 33% of operational dam failures. Gate malfunctions are another significant factor, responsible for around 13% of such failures. Both issues can lead to overtopping, which occurs when water flows over the top of the dam, eroding the structure and potentially causing catastrophic collapse. Overtopping remains one of the most common and serious contributors to dam accidents, see Figure 5 (Foster et al., 1998, 2000).

In contrast, slope failures and seismic-induced failures are significantly less common, contributing to only about 4% and 1.7% of the total operational dam failures, respectively, see Figure 5 (Foster et al., 1998, 2000). On average, one in every 180 embankment dams included in the database failed due to internal erosion, while one in every 100 experienced an internal erosion-related incident (Foster et al., 1998, 2000).

Most internal erosion failures occur within the embankment itself, often linked to features such as conduits or structural supports embedded within the fill. Importantly, incidents—defined by ICOLD as potential failures that were successfully mitigated through emergency measures like reservoir drawdown—outnumber actual failures. Internal erosion incidents are as frequently reported in dam foundations as within embankments (Fell et al., 2014).

Around two-thirds of internal erosion failures and about half of the related incidents occur during initial reservoir filling or within the first five years of operation. Nonetheless, this suggests that a significant proportion of issues arise in later operational stages. Notably, Foster et al. (1998, 2000) observed that nearly all embankment erosion failures occurred when reservoir levels reached or neared historical maximums. For foundation-related internal erosion, however, reservoir level appeared to be a less decisive factor.

Although updated data from 1970–1989 (Foster et al., 2000; ICOLD, 1995) suggest a slight reduction in recorded failure rates—possibly reflecting advances in

dam design and construction—internal erosion continues to present a significant risk. For example, in the UK, Brown & Gosden (2004) reported approximately 1,600 internal erosion-related incidents for every actual failure, with around two major events occurring annually. These figures may indicate improved surveillance and early intervention rather than a fundamental decrease in failure risk. Moreover, Regan (2009) found that the overall failure rate has remained relatively constant, highlighting that despite technical progress, seepage and internal erosion remain unresolved challenges. This complexity is further compounded by the lack of standardized classification of erosion mechanisms (Richards & Reddy, 2007), which limits the reliability of comparative failure statistics.
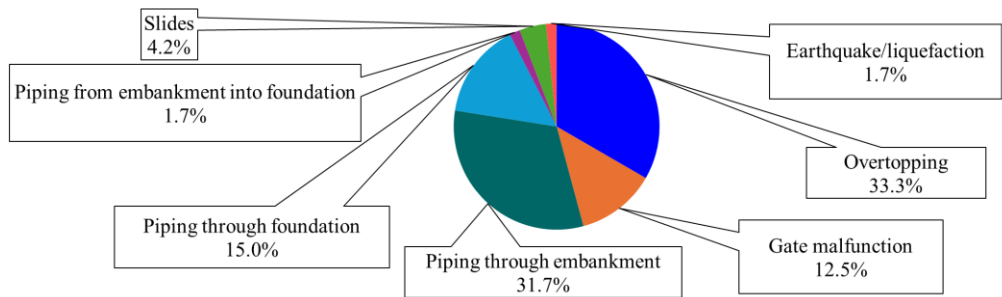
Figure 5. Dam failure statistics (Foster et al., 1998).

2.3   Internal erosion mechanisms

Fell & Fry (2007) introduced a classification scheme grounded in the fundamental mechanics governing internal erosion phenomena. This framework distinguishes four primary mechanisms: concentrated leak erosion, backward erosion piping, internal instability, and contact erosion (Bonelli & Nicot, 2013).

2.3.1   Concentrated leak erosion (CLE)

This type of erosion occurs when water flows unrestricted through a discrete opening, leading to progressive removal of soil along the boundary of the void (Figure 6). Typical examples include flow through shrinkage cracks, gaps around structural penetrations (e.g., conduits, walls, or utility lines), and animal burrows. Among all internal erosion mechanisms, CLE is considered the most hazardous, being responsible for a majority of internal erosion incidents and dam failures (Foster et al., 2000; Fry, 2016; Richards & Reddy, 2007).

2.3.2 Backward erosion piping (BEP)

This type of internal erosion typically initiates at an exposed surface on the downstream side of the dam and progresses internally or beneath the structure through the formation of channels or pipes (Figure 6) (Federico, 2017). Although it is estimated to account for about one-third of internal erosion failures (Richards & Reddy, 2007), it is notably prevalent in levee systems, with over 1,000 sand boils documented along the Mississippi River in 2011 (USACE, 2012).

2.3.3 Internal instability (II)

This process involves the removal of finer particles from a granular soil matrix by seepage flow, potentially leading to a reconfiguration of the soil structure (Figure 6). II can be categorized into suffusion (particle loss without significant volume change) and suffosion (particle loss with associated volume reduction) (Fannin & Slangen, 2014). Although typically regarded as less severe (Fry, 2016), it has received substantial attention in research due to its observable effects on embankment integrity (Rönnqvist & Viklander, 2016).

2.3.4 Contact erosion (CE)

This mechanism occurs when water flowing through a coarse material scours away an adjacent finer-grained soil (Figure 6). An example of this is found in regions like France, where fine silt embankments are constructed over gravel layers (Bonelli & Nicot, 2013; Fry, 2016). While the process tends to evolve slowly, it can result in significant material loss if flow velocities are sufficiently high.

As is evident from these descriptions, the underlying physics governing each erosion process differs substantially. II and CE primarily involve flow through porous media. In contrast, CLE is governed by channel hydraulics and the erosion resistance of exposed soil surfaces. BEP encompasses elements of both porous flow and open-channel sediment transport. Despite these distinctions, unified design principles can be applied to mitigate the risk of all four types of internal erosion (Robbins & Griffiths, 2018).
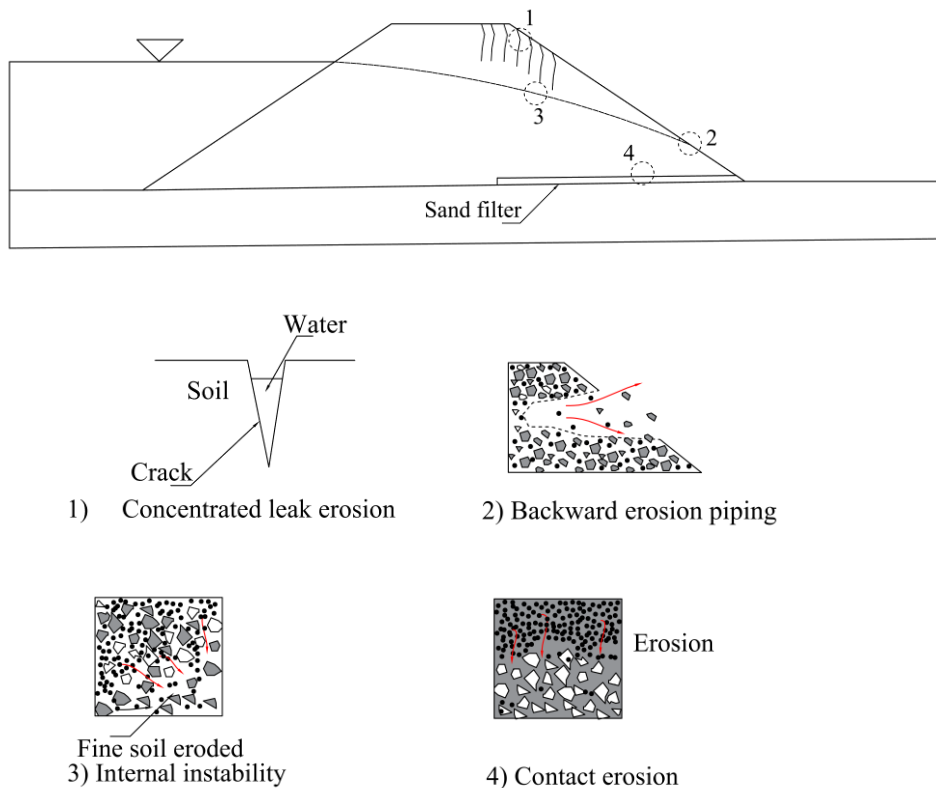
Figure 6. Schematic representation of the four internal erosion mechanisms.

2.4 Internal erosion development and detection

To better assess the development of internal erosion and identify when it becomes a critical concern, it is helpful to break the process into four main phases (Fell et al., 2014):

- initiation
- continuation
- progression
- breach

Initiation: This phase begins when the hydraulic forces within seepage flows are strong enough to detach soil particles from the dam body or foundation materials.

Continuation: Erosion continues if there are no filtering materials present along the seepage path or if there is sufficient space downstream to accommodate the

eroded particles. If the surrounding soils effectively filter the particles, the process can halt at this stage.

Progression: As erosion persists, the seepage path may enlarge into a continuous channel or "pipe." For this to happen, the surrounding soil must be stable enough to support the cavity without collapsing. The water velocity must also remain high enough to keep detaching and transporting soil particles through the unfiltered exit.

Breach: If erosion is not detected or mitigated, the dam may eventually fail. Potential breach mechanisms include pipe enlargement, crest collapse, sinkhole formation, slope failure, or structural instability.

Historical failures have shown that specific warning signs often precede piping-related failures (Foster et al., 1998). These warning signs include (Foster et al., 1998):

- increased leakage
- muddy seepage
- sinkholes
- settlement
- cracking
- sand boils
- whirlpools in the reservoir
- excess pore pressure.

The study by Foster et al. (1998) showed that increased leakage, muddy leakage, and sinkholes are common indicators of many dam failures and accidents involving internal erosion (Figure 7 and Figure 8). However, some failures and accidents can occur without any visible warning signs.
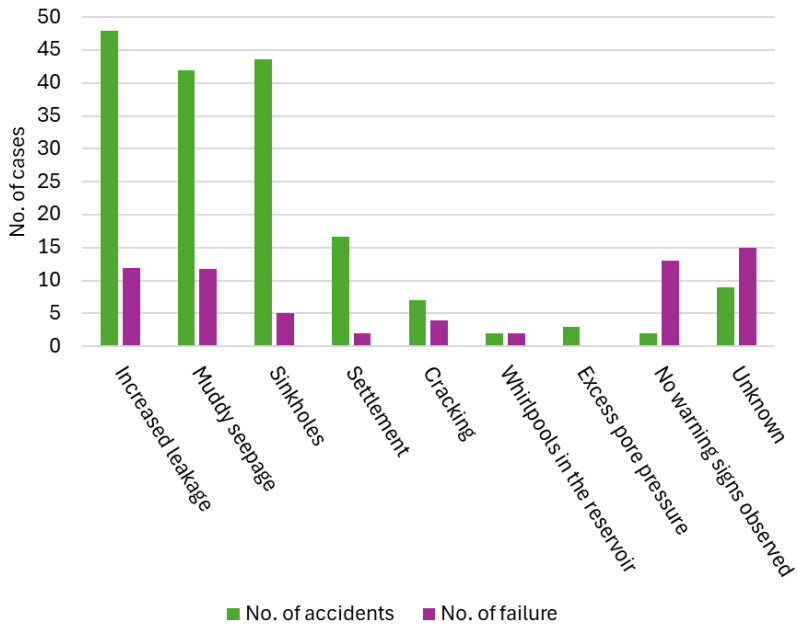
Figure 7. Observations of internal erosion through the embankment (adopted from Foster et al. (1998)).
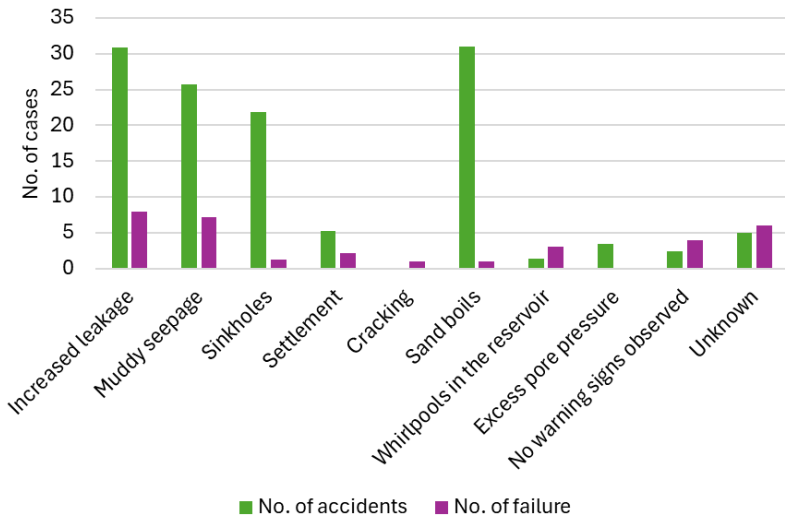
Figure 8. Observations of internal erosion through the foundation (adopted from Foster et al. (1998)).

Detecting and tracking the progression of internal erosion requires careful attention and advanced techniques capable of identifying anomalies within the dam structure before they reach a critical stage. These processes are often difficult to detect in their early stages, particularly when obscured by snow cover, vegetation, or submergence of the dam toe (Fell et al., 2003). Detection becomes especially challenging without comprehensive instrumentation and regular monitoring at appropriate intervals.

Early-stage indicators of internal erosion typically include abnormal seepage behaviour or changes in pore pressures. However, definitive confirmation usually only occurs once a visible flow path or "pipe" develops, often accompanied by settlement or measurable seepage anomalies (Fell et al., 2003). These indicators must be treated with urgency, prompting intensified surveillance and diagnostic efforts.

Although various detection methods exist, including visual inspections, seepage and pore pressure measurements, thermal sensing (e.g., fibre optics), geophysical surveys (e.g., resistivity and self-potential), and topographic deformation monitoring, the effectiveness of these techniques is contingent upon the extent and quality of the dam's instrumentation system (Fell et al., 2003). The following sections describe the most common and effective monitoring approaches currently in use.

2.5   Monitoring

Modern monitoring systems, integrating both conventional and advanced technologies, play a vital role in ensuring the safety and long-term sustainability of embankment dams.

Effective monitoring is critical throughout the entire life cycle of a dam — from the planning and design stages, through construction and initial reservoir filling, to long-term operation and maintenance. Ideally, monitoring efforts should begin as early as the planning phase to establish baseline conditions for groundwater levels and seepage behaviour (Fell et al., 2014).

Historical evidence underscores the importance of monitoring: many dam incidents that could have escalated into full-scale failures were successfully mitigated thanks to timely interventions made possible by functioning monitoring systems (Fell et al., 2014).

2.5.1   Seepage flow monitoring

Seepage monitoring is one of the most widely used methods for identifying early signs of internal erosion. It involves tracking the location, quantity, and quality of seepage through visual inspections and direct measurements (Fell et al., 2014).

Common techniques include:
- **V-notch weirs** with data loggers for continuous flow recording
- **Timed discharge measurements** into calibrated vessels
- **Chemical and biological analysis** of seepage to determine source and detect material leaching
- **Turbidity monitoring**, which is critical during the first reservoir filling, as increased turbidity may indicate the onset of piping (Fell et al., 2014).

Monitoring systems must be carefully calibrated to distinguish between normal seasonal variations (e.g., snowmelt or rainfall infiltration) and seepage anomalies caused by internal erosion.

2.5.2 Displacement monitoring

Monitoring surface displacements helps assess the structural behaviour of the dam and detect deformations associated with internal erosion or slope instability. Both vertical and horizontal movements should be recorded consistently to identify emerging patterns (Fell et al., 2014). In addition to conventional surveying methods, advanced tools have enhanced displacement tracking:
- **Global navigation satellite systems (GNSS)** offer millimetre-level accuracy
- **Synthetic aperture radar (SAR)** and **ground-based SAR** provide high-resolution, three-dimensional monitoring for remote or inaccessible sites

(ICOLD, 2014).

These advanced techniques complement traditional monitoring, enhancing dam safety and early problem detection.

2.5.3 Pore pressure monitoring

Pore pressure measurements are vital for detecting abnormal uplift forces, potential foundation heave, and irregular seepage pressure—all of which can signal internal erosion or slope instability (Fell et al., 2014). Instruments commonly used include:
- Observation wells
- Casagrande piezometers
- Hydraulic piezometers
- Pneumatic piezometers
- Vibrating wire piezometers

Although piezometers are particularly effective in cohesionless foundations with low-permeability covers, their routine use in embankment cores is discouraged due to low capture probability for leaks and potential construction-related risks. Instead, they are better suited for foundation monitoring, especially where no positive cutoffs are present (Fell et al., 2003).

2.5.4 Thermal monitoring

Thermal sensing is used to detect and quantify seepage flow based on temperature gradients within the dam structure. Internal seepage alters expected thermal patterns, offering insights into hidden leakage paths. Techniques include (Fell et al., 2014):

- **Distributed fibre optic temperature sensing (DTS):** Fibre optic cables are installed in key locations such as downstream toes, or drainage galleries. These systems are robust, interference-free, and suited for continuous, high-resolution monitoring.
- **Thermotic sensors in standpipes:** Installed at depths up to 30–40 m, these sensors detect vertical temperature gradients. In coarse soils, spacing may be increased; however, convection within wide standpipes can distort readings.
- **Infrared imaging:** Trialled primarily on downstream faces, this method is more sensitive to ambient temperature effects and thus less reliable than other thermal techniques.

2.5.5 Geophysical methods

Geophysical surveys complement traditional monitoring by identifying internal moisture anomalies, grain size effects, and potential erosion pathways. Techniques such as:

- **Electrical resistivity**
- **Self-potential surveys**

are effective in detecting moisture accumulation, grain size variations, and subsurface changes without the need for intrusive drilling (Fell et al., 2014). These methods are particularly valuable in large dam foundations or in vegetated and inaccessible areas.

Compared to purely visual inspections or isolated point measurements, geophysical techniques provide spatially continuous data that can reveal hidden defects before they manifest at the surface. Among these methods, ERT is particularly well-suited for detecting variations in water content and permeability within the dam body, while IP can offer additional insight into soil texture and mineral composition, helping to distinguish between fine-grained materials and coarse zones. The combination of ERT and IP thus enables both the identification of seepage paths and the characterization of materials, making them powerful tools for understanding and mitigating internal erosion risks. For this reason, these two techniques have been selected for further development and application in this thesis.

3 Methods and material

This chapter provides an overview of the materials and methodologies used in this study to evaluate monitoring techniques for embankment dams, focusing on ERT and IP. In addition, the chapter introduces seepage modelling as a complementary analytical tool used to simulate water movement within the dam structure.

The chapter is divided into several sections, each focusing on a specific aspect of the study. It begins by introducing the principles and practical application of resistivity measurements in dam monitoring. This is followed by a discussion of IP, emphasizing its theoretical foundation and its relationship to resistivity. Additional sections are devoted to forward modelling, inversion modelling, and the strategies employed for data filtering. The chapter also presents the methodology for seepage modelling, where material parameters are derived from ERT data.

3.1   Resistivity

Resistivity measurement is a geophysical method used to determine the electrical resistivity of the ground by applying an electric field and measuring the resulting voltage. This method is particularly useful for investigating geological formations and material properties beneath the surface, such as moisture content, mineralogy, and porosity (Loke, 2002).

In the field measurements a known current I is introduced into the ground using a pair of current electrodes (commonly labeled A and B), and the resulting voltage difference ΔV is measured between a pair of potential electrodes (M and N) (Figure 9). The apparent resistivity ρ_a is then calculated using the geometric factor K, which depends on the electrode configuration (Loke, 2002):

$$\rho_a = K.\frac{\Delta V}{I} \tag{1}$$

The geometric factor K for a general electrode configuration is given by (Loke, 2002):

$$K = 2\pi \left(\frac{1}{AM} - \frac{1}{BM} - \frac{1}{AN} + \frac{1}{BN} \right)^{-1} \tag{2}$$

where AM is the distance between electrodes A and M, BM is the distance between electrodes B and M, etc.

$\rho_1 > \rho_2$

⟶ Current-flow lines
------ Equipotentials
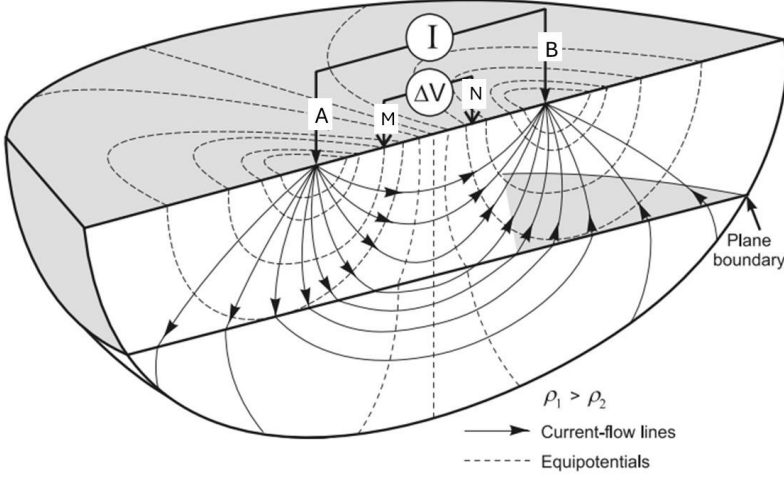
Figure 9. Single resistivity measurement (adopted from Knödel et al. (2007)).

In practice, a resistivity meter is used to inject current and record voltage responses. By conducting multiple measurements across the survey area, a resistivity profile of the subsurface can be established. In ERT, arrays of electrodes are deployed to acquire either two-dimensional (2D) or 3D data. A 2D ERT survey provides a vertical cross-section along a line, capturing both depth and horizontal variations along the profile, but it cannot resolve variations perpendicular to the survey line. In contrast, 3D ERT involves a grid or multiple intersecting lines of electrodes, allowing resistivity variations to be resolved in all three spatial directions. In this study, 3D measurements with different electrode array configurations were employed to enhance resolution and provide a more comprehensive representation of subsurface conditions within the dam.

It is important to note that the measured values represent *apparent resistivity*, not the true resistivity distribution. Apparent resistivity corresponds to the equivalent homogeneous half-space that would produce the same voltage response for a given electrode configuration. The relationship between apparent and true resistivity is non-linear and spatially variable, making the problem inherently complex. To

overcome this, inversion techniques are applied to reconstruct the true resistivity distribution from the field data.

Finally, the physical basis for resistivity measurements can be described by a fundamental equation derived from Ohm's law and the principle of current conservation (Dey & Morrison, 1979):

$$\nabla . (\sigma \nabla \varphi) = -I\delta(\boldsymbol{r} - \boldsymbol{r_s}) \tag{3}$$

Where σ is the electrical conductivity (S/m), φ is the electric potential (V), I is the injected current (A), δ is the Dirac delta function, $\boldsymbol{r_s}$ is the location of the current source. This Poisson equation governs the spatial distribution of the electric potential in a conductive medium. For simple geometries, such as a point source in a homogeneous half-space, analytical solutions exist and form the classical basis for resistivity methods. For more complex conductivity distributions, however, the equation must be solved numerically, typically using finite difference or finite element methods, to model the potential field.

3.2   Induced Polarization (IP)

IP is a geophysical phenomenon describing the temporary storage and delayed release of electric charge in soils and rocks when an external electric field is applied. Unlike direct current (DC) resistivity methods, which assume purely ohmic conduction, IP accounts for the capacitive and electrochemical behaviour of porous media (Binley & Slater, 2020). These processes are typically associated with fluid–solid interfaces, where ions accumulate within the electrical double layer (EDL) at mineral surfaces, in pore throats, or around metallic minerals. This accumulation of charge creates a polarization effect that produces either a measurable voltage decay after the current is switched off or a frequency-dependent resistivity response.

Electrical conduction in porous media occurs through two primary mechanisms: (i) ionic transport in the electrolyte that saturates the interconnected pore space, commonly referred to as electrolytic conduction (σ_{el}), and (ii) charge transport within the electrical double layer at mineral–fluid interfaces, known as surface conduction (σ_{surf}). The effective bulk conductivity (σ) of a porous medium therefore reflects not only the intrinsic properties of the fluid and solid phases, but also the geometry of the conduction pathways, including pore connectivity, tortuosity, and the distribution of conductive minerals. A common simplifying assumption is a parallel configuration, which leads to the following relation (Waxman & Smits, 1968):

$$\sigma = \sigma_{el} + \sigma_{surf} \tag{4}$$

Under fully saturated conditions, the electrolytic conductivity is proportional to the conductivity of the pore fluid (σ_w):

$$\sigma_{el} = \frac{1}{F}\sigma_w \tag{5}$$

where F is the formation factor (Archie, 1942). This factor is linked to the interconnected porosity and the tortuosity of the pore network.

Surface conductivity, on the other hand, depends on factors such as the specific surface area (or grain/pore size distribution), the electrochemical properties of the EDL, and the tortuosity of the connected surfaces. In laboratory experiments, multi-salinity measurements are often conducted to estimate F and σ_{surf}. This is achieved through the linear relationship obtained by substituting equation (5) into equation (4) (Rink, 1974; Waxman & Smits, 1968):

$$\sigma = \frac{1}{F}\sigma_w + \sigma_{surf} \tag{6}$$

The electrical conduction and polarization properties of the subsurface can be represented through the concept of complex conductivity, which consists of a real part (σ', associated with conduction) and an imaginary part (σ'', associated with polarization):

$$\sigma^* = \sigma' + i\sigma'' \tag{7}$$

Accordingly, the real and imaginary parts of the measured complex conductivity are:

$$\sigma' = \sigma_{el} + \sigma'_{surf} = \frac{1}{F}\sigma_w + \sigma'_{surf} \tag{8}$$

$$\sigma'' = \sigma''_{surf}$$

IP measurements are commonly performed in either the time-domain or the frequency-domain. In the time-domain IP (TDIP), a DC is applied to the ground, and after it is switched off, the decay of the resulting voltage is recorded. The delayed voltage response indicates the presence of polarizable materials. In contrast, frequency-domain IP (FDIP) involves applying an alternating current (AC) and measuring the frequency-dependent variation in apparent resistivity or the phase lag between voltage and current. Although these approaches differ in measurement technique, they are theoretically equivalent, as both capture the same underlying polarization processes in the subsurface (Loke, 2002).

For TDIP, the principal parameter is the chargeability, typically defined as (Loke, 2002):

$$m_t = \frac{1}{V_{DC}} \int_{t_1}^{t_2} V_s(t) dt \qquad (9)$$

where V_{DC} is the steady-state voltage before the current is switched off, and $V_s(t)$ is the voltage measured during the decay interval $[t_1, t_2]$. The resulting chargeability values are usually expressed in millivolts per volt (mV/V) or milliseconds (ms).

It is important to note that the resulting chargeability depends on the chosen time gates (t_1 and t_2), and therefore may not be quantitatively consistent between different surveys or instruments. Early times in the decay curve can be influenced by inductive coupling, which is usually removed or corrected during data processing. Various approaches exist to process IP decays, including stacking, filtering, and curve-fitting, in order to extract reliable chargeability values from noisy or distorted measurements.
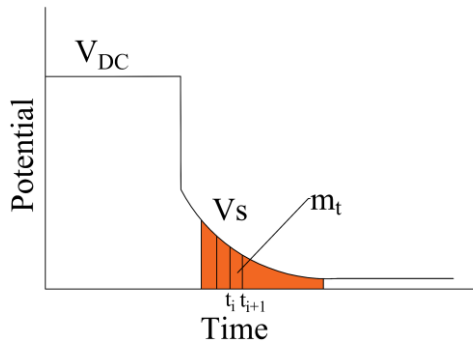
Figure 10. TDIP measurements (adopted from Revil et al. (2022)).

IP is sensitive to subsurface properties including grain size distribution, surface area, porosity, water content, and the presence of conductive or polarizable minerals. These dependencies make IP a valuable tool in mineral exploration, environmental studies, and geotechnical investigations.

3.3   Forward modelling

Forward modelling is a fundamental component of geophysical methods, particularly in electrical resistivity surveys. In the context of DC resistivity, forward modelling involves computing the expected voltage measurements at the surface

electrodes, given a known subsurface distribution of resistivity and a specific electrode configuration. This is achieved by solving the governing physical equations that describe how electric current flows through the Earth's materials, see Equation (3). The process can be represented as:

$$\mathbf{d}_{calc} = \mathbf{F}(\mathbf{m}) \tag{10}$$

where $\mathbf{d}_{calc}$ is the calculated data, $\mathbf{F}$ is the forward modelling operator and $\mathbf{m}$ is the model parameter vector (e.g., resistivity values).

To represent the complex and often heterogeneous subsurface, the model domain is discretized into layers (in 1D) or a grid of cells (in 2D or 3D), with each unit assigned a constant resistivity value. For each current injection configuration, the resulting electric potential at the measurement electrodes is computed. The process typically uses either finite difference or FE numerical methods to approximate the solution of the governing equations, as analytical solutions are rarely feasible for real-world cases. These simulated data form the basis for comparison with actual field observations, making forward modelling an essential step in both data interpretation and inversion (Binley & Slater, 2020).

Beyond its role in inversion, forward modelling is also a powerful tool in survey planning and experimental design. By simulating different electrode configurations and resistivity distributions, researchers can evaluate the sensitivity of various measurement configurations to subsurface features. This enables optimization of array types and electrode spacing to improve resolution and minimize ambiguity in the data. In 2D and 3D scenarios, especially, the forward modelling process often involves solving a large number of equations, particularly when multiple current sources are involved. This has historically posed significant computational challenges, though advances in numerical algorithms, unstructured meshing, and hardware capabilities have made large-scale modelling increasingly accessible. Moreover, methods like 2.5D modelling, which account for 3D current flow while assuming 2D resistivity variation, provide a practical compromise between computational efficiency and physical realism. Today, forward modelling is not only a critical step for fitting models to data but also a strategic tool for enhancing the design, efficiency, and interpretability of resistivity surveys (Binley & Slater, 2020).

In this study, forward modelling is conducted using the Python Boundless Electrical Resistivity Tomography (pyBERT) and Python Geophysical Inversion and Modelling Library (pyGIMLi) software package (Rücker et al., 2017). Various electrode configurations and combinations are evaluated by generating synthetic data through forward modelling prior to the field measurements. The synthetic data are then inverted to assess whether the resulting models are capable of detecting the expected defects, thereby ensuring the suitability of the survey design.

3.4 Inversion modelling

Inverse modelling in ERT seeks to estimate a subsurface resistivity distribution $\mathbf{m}$ that best explains the observed data $\mathbf{d}$ (e.g., apparent resistivity) through a forward operator $\mathbf{F}$. The forward problem is defined as $\mathbf{d}=\mathbf{F}(\mathbf{m})$, and the inverse problem aims to find $\mathbf{m}$ such that $\mathbf{m}=\mathbf{F}^{-1}(\mathbf{d})$. Because $\mathbf{F}$ is typically nonlinear, the inverse problem is solved iteratively using linearization techniques such as the Gauss–Newton method. At each iteration k, the model is updated by solving the linearized system (Binley & Slater, 2020):

$$\mathbf{J}_k^T \mathbf{W}_d^T \mathbf{W}_d \mathbf{J}_k \Delta \mathbf{m}_k = \mathbf{J}_k^T \mathbf{W}_d^T \mathbf{W}_d (\mathbf{d}_{obs} - \mathbf{F}(\mathbf{m}_k)) \tag{11}$$

where $\mathbf{J}_k$ is the Jacobian matrix containing partial derivatives of the data with respect to the model parameters, $\Delta \mathbf{m}_k$ is the model update, and $\mathbf{W}_d$ is the data weighting matrix that accounts for measurement uncertainties. The iterative update is then $\mathbf{m}_{k+1} = \mathbf{m}_k + \Delta \mathbf{m}_k$. Due to the ill-posed and non-unique nature of inverse problems, constraints and regularization are essential to obtain physically meaningful and stable solutions.

To stabilize the inverse solution and prevent overfitting to noisy data, regularization is commonly introduced through a penalty function that incorporates prior assumptions about model smoothness. One popular form is Tikhonov regularization, where the objective function to be minimized (Tikhonov & Arsenin, 1977):

$$\Phi(\mathbf{m}) = \|\mathbf{W}_d(\mathbf{d}_{obs} - \mathbf{F}(\mathbf{m}_k))\|^2 + \alpha^2 \|\mathbf{W}_m \mathbf{m}\|^2 \tag{12}$$

where α is the regularization parameter and $\mathbf{W}_m$ is the model roughness operator, often approximating the second spatial derivative. The solution can be obtained via a damped Gauss–Newton scheme, also known as the Levenberg–Marquardt method (Binley & Slater, 2020):

$$(\mathbf{J}^T \mathbf{W}_d^T \mathbf{W}_d \mathbf{J} + \alpha^2 \mathbf{W}_m^T \mathbf{W}_m) \Delta \mathbf{m} = \mathbf{J}_k^T \mathbf{W}_d^T \mathbf{W}_d (\mathbf{d}_{obs} - \mathbf{F}(\mathbf{m})) \tag{13}$$

The value of α is often chosen through methods like the L-curve criterion or line search, balancing data misfit and model roughness. This formulation ensures convergence towards a smooth model that still fits the data within the prescribed noise level. While L2-norm regularization promotes smooth solutions, alternatives such as L1-norm or pseudo-L1 regularization may be employed to recover blocky features and sharp boundaries, making them more suitable for heterogeneous subsurface conditions (Binley & Slater, 2020).

ERT measurements are commonly conducted using a 2D approximation, whereas full 3D measurements are primarily applied in research contexts. The 2D approach is relatively cost- and time-efficient, and allows for easy deployment of electrodes.

However, traditional 2D surveys assume that current flow is confined to a vertical plane, whereas in reality it spreads in all directions. Ignoring this can lead to projection artefacts, emphasizing the value of incorporating 3D measurements. Data acquisition for 3D studies typically involves arranging electrodes in a grid or, more commonly, combining multiple parallel 2D survey lines into a single quasi-3D inversion framework (Cheng et al., 2019). Historically, the implementation of 3D inversion was challenging due to the high computational and storage demands of the Jacobian matrix, leading many studies to omit full 3D measurements (Sasaki, 1994). However, advances in computational power, efficient solvers, parallel computing, and unstructured meshing have made 3D inversion increasingly feasible, allowing ERT to accurately account for the true 3D distribution of current flow in the subsurface (Johnson et al., 2010).

In addition to spatial complexity, time-lapse (or four-dimensional (4D)) inversion has been developed to monitor dynamic subsurface processes, such as changes in saturation, salinity, or temperature (LaBrecque & Yang, 2001). Unlike standard inversions that treat each dataset independently, time-lapse inversion exploits temporal correlations between successive measurements to isolate real changes in subsurface resistivity from static background features. Common approaches include difference inversion and ratio methods (Daily et al., 1992; LaBrecque & Yang, 2001) which suppress inversion artefacts and enhance sensitivity to temporal variations. More advanced strategies employ joint spatiotemporal regularization, promoting smoothness both in space and time (Karaoulis et al., 2011), thereby improving the robustness and interpretability of time-lapse studies.

3D effects, such as those introduced by embankment dam slopes, heterogeneity in internal material properties that result in varying resistivity, and irregular surface topography, can lead to distortions in the ERT data. These effects challenge one of the fundamental assumptions in traditional 2D ERT processing: that the subsurface is laterally homogeneous and extends infinitely perpendicular to the electrode line. When these conditions are not met, as discussed by Sjödahl et al. (2005), the calculated geometric factors may become inaccurate, leading to potential misinterpretation of the resistivity models. Thus, it is necessary to consider the distortions and the induced errors in inverse modelling. Hence, researchers used different techniques such as 3D calculations of the geometric factors and 3D inversion models to consider the distortions due to 3D effects (Bièvre et al., 2018; Cho et al., 2014; Fargier et al., 2014; Norooz et al., 2021).

The Python-based software package pyBERT/pyGIMLi is also used for the inversion of both ERT and IP data. In this study, both 3D time-lapse and single-time inversion models are applied, incorporating 3D geometric factor calculations to enhance the accuracy of the results.

Around 200 000 cells were generated for the inversion model using the TetGen software (Si, 2015) (Figure 11).
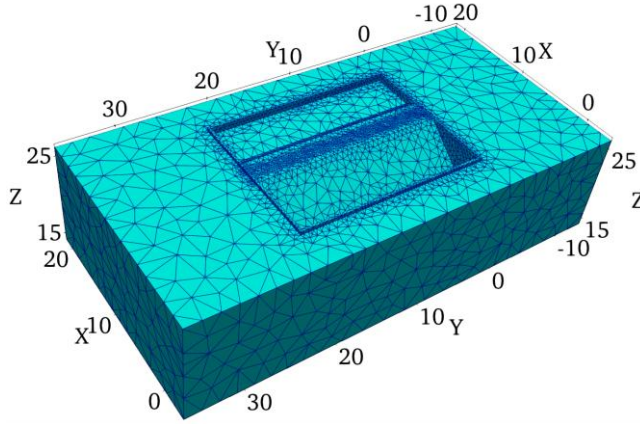
Figure 11. The generated mesh for the inversion model.

To avoid smooth transitions and consider the expected sharp transitions between the dam zones, robust (L1) method was applied. 12 regions were simulated in the geometry of the model which are shown in Figure 12.
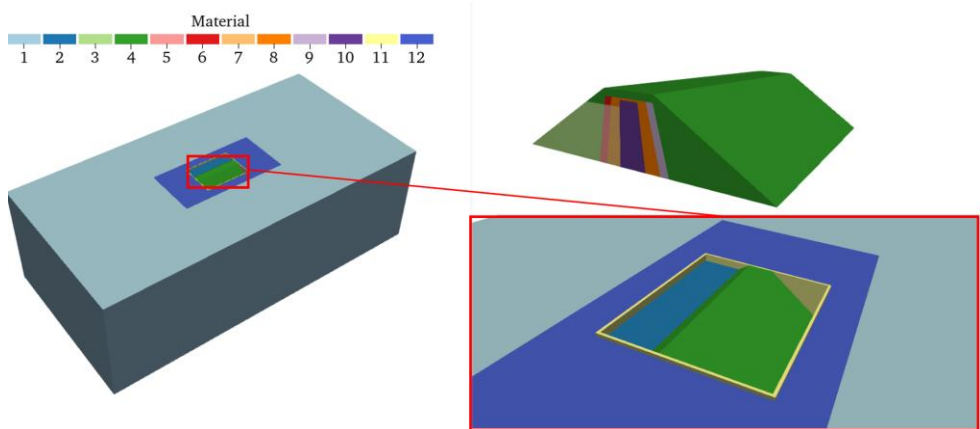
Figure 12. Inversion model geometry separated into distinct regions.

3.5   ERT and IP data quality

Reciprocal analysis is a widely used technique to assess measurement reliability and quantify errors in both ERT and IP data (Udphuay et al., 2011). In this study, to evaluate the quality of the geophysical measurements, a total of 1,547 reciprocal

measurements were conducted during the survey period, representing approximately 11% of the daily collected data.

For ERT, the reciprocal error is calculated using the relative difference between two measurements with reversed current and potential electrode pairs:

$$Reciprocal\ error_{resistivity} = \left| \frac{R_1 - R_2}{(R_1 + R_2)/2} \right| \times 100 \tag{14}$$

where R_1 is the measured resistivity when electrodes **A** and **B** are the current electrodes, and electrodes **M** and **N** are the potential electrodes. R_2 is the measured resistivity when electrodes **M** and **N** are the current electrodes and electrodes **A** and **B** are the potential electrodes.

The result is expressed as a percentage and provides a relative estimate of measurement error.

For IP data, reciprocal error is calculated using the absolute difference between two chargeability values obtained from reversed electrode configurations:

$$Reciprocal\ error_{IP} = |M_1 - M_2| \tag{15}$$

Where M_1 and M_2 are the chargeability values (in ms) from reciprocal measurements.

This simplified approach avoids potential instabilities caused by divisions with small or zero apparent chargeability values—issues that are common in IP measurements due to their low signal amplitude. As a result, it provides a more reliable indicator of data quality in IP surveys.

3.6 Electrode array configuration

The choice of measurement arrays has a direct impact on the sensitivity distribution and coverage of ERT data. In ERT, sensitivity is typically concentrated in the regions between the current electrodes and decays with distance from the source–receiver quadrupole (Binley & Slater, 2020). Different array geometries emphasize different parts of the subsurface, and by combining multiple arrays it is possible to achieve complementary coverage and improved resolution of heterogeneous structures. In this study, the following arrays were employed:

Bipole–bipole array (Bing & Greenhalgh, 2000)**:** In this configuration, current is injected into the ground through two electrodes separated by a fixed distance, while the resulting voltage is measured between a separate pair of electrodes. These potential electrodes are typically positioned either on the same line or on a parallel line relative to the current electrodes. It provides good depth penetration and sensitivity to vertical changes, but may have lower resolution for lateral features.

Multiple gradient array (Dahlin & Zhou, 2006)**:** This array combines measurements at various spacings and positions to increase data redundancy and improve both lateral and vertical resolution. The trade-off is increased complexity in data acquisition and processing.

Extended gradient array (Zhou et al., 2020)**:** In this array, multiple potential measurements are taken along an extended line from the current electrodes. It enhances lateral resolution and is effective for mapping gradual subsurface changes. However, it may require longer survey times and careful electrode placement.

Corner arrays (Tejero-Andrade et al., 2015)**:** These arrays are used to target complex geometries or boundaries, such as the edges of a dam core or filter zones. By positioning electrodes at corners and along inclined lines, deeper or otherwise hard-to-detect anomalies can be resolved. Corner arrays are especially useful near structural transitions, but are more labour-intensive to deploy and may require careful planning to avoid measurement errors.

By selecting an appropriate combination of these arrays, ERT surveys can be optimized to provide comprehensive coverage of the dam structure, while balancing resolution, depth, and efficiency.

3.7 Data filtering and processing

Typically, manual data quality control and filtering are performed after data collection by checking for outliers and removing this. However, in this case, the large number of data points, the 3D approach and time series with daily datasets for 4.5 years make manual filtering impractical. Therefore, an automated data filtering approach is employed in this thesis.

3.7.1 Preprocessing of IP data

In the first step, the raw IP data were pre-processed using the workflow introduced by Olsson et al. (2016). This method provides a comprehensive chain of noise removal and correction steps designed to improve the signal-to-noise ratio and extend the usable temporal spectrum of IP data. The key stages are:

1. Harmonic de-noising: modelling and removing the fundamental power-line frequency and its harmonics, thereby recovering early-time data in the millisecond range.
2. Spike removal: identification and suppression of isolated spikes caused by transient disturbances, which would otherwise distort the decay curves.
3. Drift correction: instead of applying a simple linear correction, drift is modelled and removed using a Cole–Cole relaxation function, which preserves the shape of the true IP response at late times.

4. Tapered gating: decay curves are segmented into logarithmically increasing time windows with tapered edges, which reduces overlap with harmonic noise and provides more efficient sampling of the signal.
5. Uncertainty estimation: data variance within each gate, combined with the fit quality of the drift model, is used to quantify IP data errors, which are crucial for appropriate weighting during inversion.

This preprocessing effectively doubled the usable temporal spectrum of IP (about four decades of time), allowing both early- and late-time responses to be analysed with higher accuracy. Importantly, the full waveform data are preserved throughout the preprocessing workflow, ensuring that no information from the raw measurements is lost. As a result, the IP data quality was greatly enhanced, providing a robust basis for subsequent filtering and inversion.

3.7.2 Temporal filtering of ERT/IP data

Two different types of temporal filtering techniques were applied to the time-series measurements in this study following the preprocessing step. To ensure data quality and reliability prior to inversion, a comprehensive strategy for temporal filtering and outlier handling was implemented.

Infinite Impulse Response (IIR) Low-Pass Filtering

The first filtering method applied a bidirectional IIR low-pass filter to smooth the data over time, following the approach proposed by Sjödahl et al. (2008). In this method, each data point is updated through a weighted average where the smoothing factor *f* controls the influence of surrounding values. The backward filtering step is defined by:

$$y_i^{backward} = \frac{y_{i-1} + f x_i}{1 + f} \tag{16}$$

where x_i is the raw data, y_{i-1} the previously filtered value, and *f* the smoothing coefficient. To limit abrupt transitions, a maximum relative change constraint was applied:

$$y_i^{backward} = clip(y_i^{backward}, y_{i-1} - max_{impact} \cdot |y_{i-1}|, y_{i-1} + max_{impact} \cdot |y_{i-1}|) \tag{17}$$

This process was repeated in the forward direction, and the final output was calculated by averaging both passes, thus reducing phase distortion. For this study, the smoothing factor *f* was set to 0.2 and the maximum impact to 0.4.

Enhanced Low-Pass Filtering with Pre-smoothing

To further enhance the data quality, the low-pass filtering method with pre-smoothing was implemented as the second filtering technique. This strategy aimed to preserve long-term trends while effectively suppressing short-term fluctuations. As a preliminary step, all resistivity and chargeability values falling outside the physically plausible ranges—5 to 10 000 Ω·m for resistivity and ±250 ms for chargeability—were removed. This decision was motivated by the observation that a small number of raw data points exceeded these thresholds. The filtering procedure was then conducted in two main phases:

a. Pre-smoothing using a Rolling Median Filter: A rolling median filter with a window size of 7 was first applied to each time series. This non-linear filter replaces each data point with the median value within a sliding window, thereby preserving sharp transitions while removing isolated outliers (Gabbouj et al., 1992).

b. Bidirectional IIR low-pass filtering: Following pre-smoothing, the IIR low-pass filter, as previously described, was applied in both forward and backward directions with f set to 0.4 in this phase. The bidirectional results were then averaged to minimize phase distortion. A maximum impact parameter (0.4) was introduced to constrain the rate of change between consecutive points, increasing robustness against transient anomalies and ensuring a consistent temporal profile across all data series.

3.8   Seepage Modelling

Transient seepage in embankment dams is a critical phenomenon affecting their stability and safety. Understanding how water moves through variably saturated, heterogeneous, and anisotropic soils is essential for predicting pore pressures, assessing seepage rates, and evaluating the potential for internal erosion or piping. The governing equation for transient seepage in nonhomogeneous, anisotropic soil is derived from the principles of mass conservation and Darcy's law. It can be expressed as (Richardson, 2007):

$$\frac{\partial}{\partial x}\left(-k_x \frac{\partial h}{\partial x}\right) + \frac{\partial}{\partial y}\left(-k_y \frac{\partial h}{\partial y}\right) + \frac{\partial}{\partial z}\left(-k_z \frac{\partial h}{\partial z}\right) = \frac{\partial \theta}{\partial t} \tag{18}$$

where h is the pressure head (m) and k_x, k_y, and k_z are the hydraulic conductivity of the soil in the x, y, and z directions, respectively, expressed in meters per second (m/s). The symbol θ is the volumetric water content of the soil mass (–), and t is time (s).

This partial differential equation describes how water moves through a variably saturated anisotropic porous medium. Due to the complexity of natural boundaries and soil heterogeneity, analytical solutions are often not feasible. Therefore, various

numerical methods are employed to solve it. Among these, the Finite Element Method (FEM) is widely recognized for its flexibility and accuracy, particularly in cases involving complex geometries and heterogeneous materials. Other commonly used methods include the Finite Difference Method (FDM) (Smith, 1985), known for its simplicity in structured grids, and the Boundary Element Method (BEM) (Brebbia, 1984), which is effective in problems with infinite or semi-infinite domains. These methods each offer distinct advantages depending on the specific conditions and modelling requirements.

In this study, SEEP3D, a FE module within the GeoStudio software suite, was used to model transient seepage through the Älvkarleby test dam. The primary objective of the modelling was to simulate water flow under varying hydraulic conditions, predict pore pressure distribution, and assess seepage behaviour in heterogeneous and anisotropic soil layers. This approach provides a reliable and practical framework for analysing the dam's hydromechanical response under transient conditions.

The generated mesh in the SEEP3D program is shown in Figure 13. Approximately 22 000 cells were created, balancing convergence accuracy and computational efficiency. Various mesh sizes were tested, and the final mesh size was selected based on the point at which further refinement no longer affected the results.
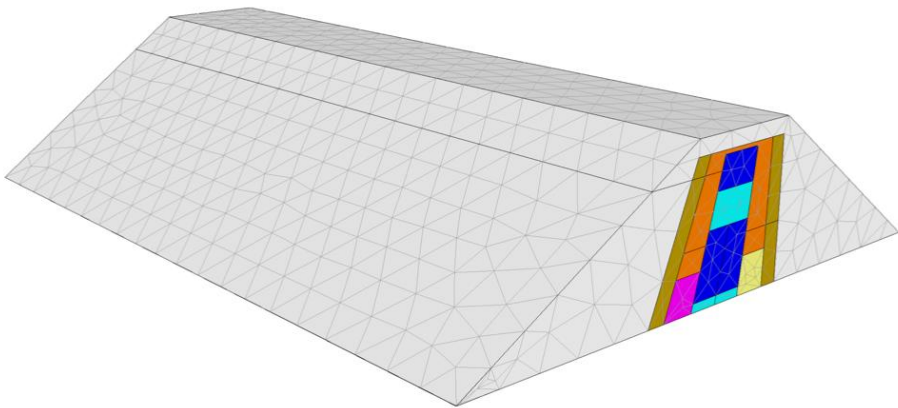

Figure 13. The generated mesh for the seepage model.

48

4 Älvkarleby test dam

The Älvkarleby test embankment dam, located in Sweden, was designed as a key research site for evaluating various monitoring techniques, particularly non-invasive geophysical methods. This chapter provides a detailed overview of the dam's structure, including its cross-section, construction materials, and internal zoning. It also outlines the deployment of 3D ERT and IP surveys aimed at identifying internal defects. The chapter also describes the measurement setup, including electrode configuration and data acquisition strategies. In addition to the geophysical methods, complementary measurements are presented—such as pore pressure monitoring, turbidity analysis, and laboratory testing of particle size distribution—to provide a more comprehensive understanding of the dam's internal conditions and seepage behaviour.

4.1 Älvkarleby embankment dam

Vattenfall R&D (VRD) has constructed the test embankment dam at their research facility in Älvkarleby, located in eastern Sweden (see Figure 14) (Bernstone et al., 2021). The dam was situated within a concrete container measuring 20 m in length, 16 m in width, and 4 m in height. It served as a scaled-down representation of a conventional Swedish embankment dam, featuring internal zoning that included a hydraulically sealed core of fine-grained till, flanked by layers of fine and coarse filters, as well as structural fill material (Figure 15a).

Figure 14. Aerial view of Älvkarleby test dam (Bernstone et al., 2021).
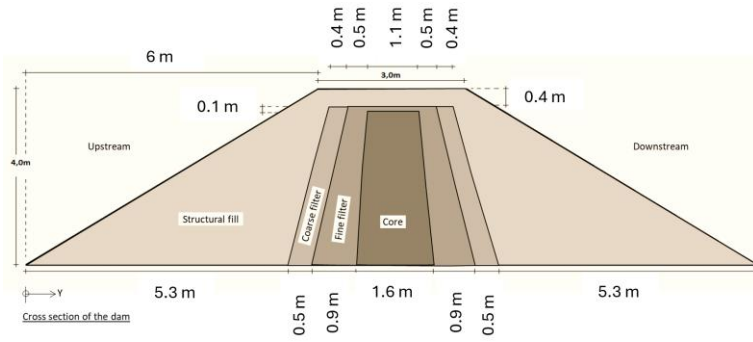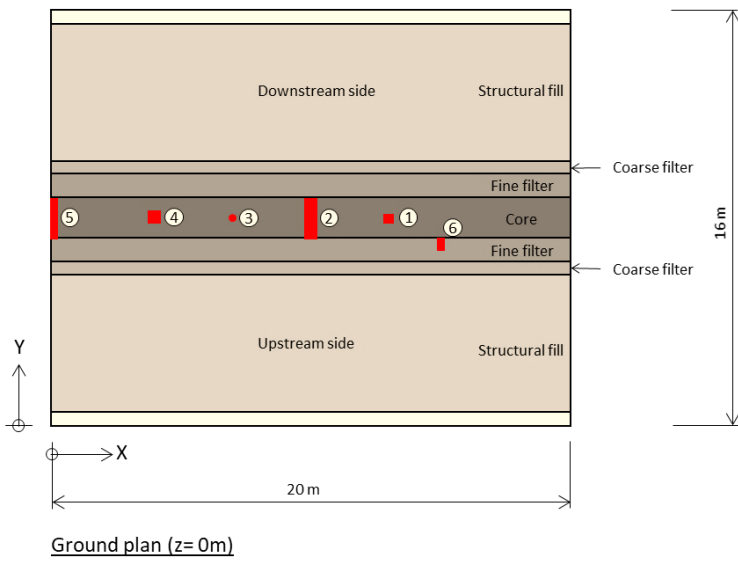
Figure 15. a) Cross-section of Älvkarleby test dam; b) Ground plan of the dam with defects in red; c) Cross-section of core from upstream (y≈6.7 m) with defects in red (modified from Lagerlund et al., 2022).

In November 2022, an injection procedure was performed using magnetite-containing materials in two locations, selected for their potential magnetic properties to facilitate detection via geophysical techniques. The injections aimed to assess their effectiveness in remediating defects within the dam body. The exact locations are indicated in Figure 16.
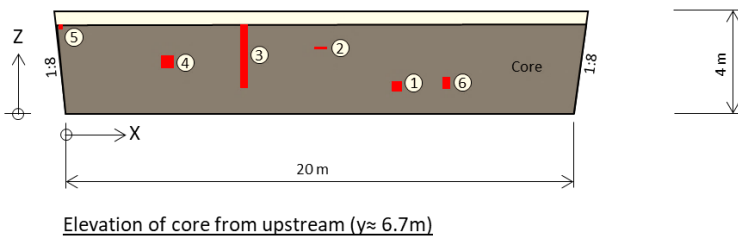
Casing pipes were installed and the contained soil was removed to a depth of approximately 3.5 m below the crest. During the injection process, the pipes were progressively withdrawn while grout was pumped in under pressure. The resulting height of the injection column differed among the boreholes, depending on factors such as applied injection pressure and local site conditions.
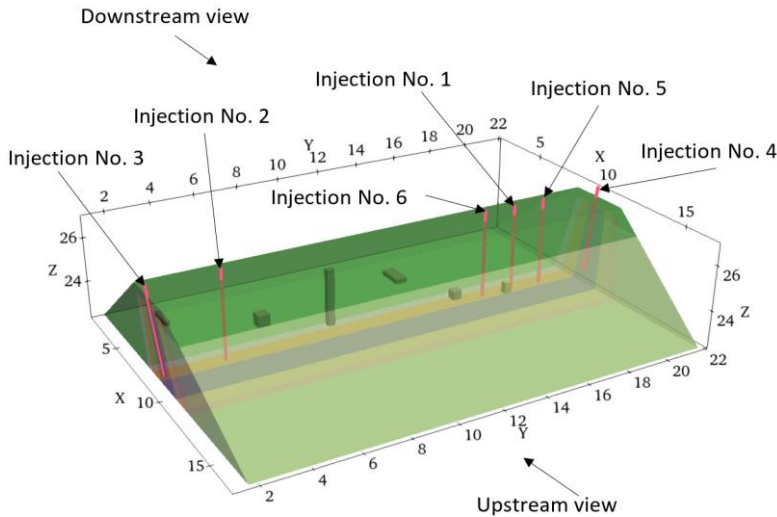
Figure 16. The location of the injections within the dam structure.

4.2   Internal defects and their characteristics

A number of intentionally introduced small-scale defects were embedded within the dam's core and fine filter zones (highlighted as red rectangles in Figure 15b and Figure 15c). The introduced defects include: a wooden block mimicking a void (Defect 1 in Figure 15b, Figure 15c, Figure 17a and Table 1); two horizontally oriented permeable layers (Defects 2 and 5 in Figure 15b, Figure 15c, Figure 17b and Table 1); a vertically oriented zone of loosened material (Defect 3 in Figure 15b, Figure 15c, Figure 17c and Table 1); and a concrete lump intended to represent a stone inclusion (Defect 4 in Figure 15b, Figure 15c, Figure 17d and Table 1). Additionally, a filter-related defect was installed in the fine filter area (Defect 6 in Figure 15b, Figure 15c, Figure 17e and Table 1). While Defects 2, 3, and 5 were

specifically designed to mimic internal erosion, the remaining anomalies were included to introduce material inhomogeneities.

Figure 17. The defects incorporated inside the core and filter; a) The cavity in the core (Defect No. 1); b) The horizontal permeable zones in the core (Defects No. 2 and 5); c) The vertical loose zone in the core (Defect No. 3); d) The lump of concrete in the core (Defect No. 4); e) The filter defect (Defect No. 6) (Lagerlund et al., 2022).

Table 1. Description and placement of defects introduced in the test dam structure (Lagerlund et al., 2022).

Defect No.	Description	Simulated Feature	Orientation	Dimensions (L × W × H) (cm)	Installed Zone
1	Wooden block	Cavity	-	40 × 30 × 15	Core
2	Sand-filled layer	Permeable zone	Horizontal	140 × 40 × 5	Core
3	Loosely packed sand	Weak vertical zone	Vertical	50 × 30 × 30	Core
4	Concrete lump	Stone/block inclusion	-	40 × 30 × 20	Core
5	Sand-filled layer	Permeable zone	Horizontal	140 × 40 × 5	Core
6	Local removal of filter material	Filter defect	Horizontal	30 × 30 × 15	Fine filter

4.3   Complementary measurements

In this experiment, turbidity, water temperature, and leakage rates were measured. Leakage and turbidity through the dam were monitored over time across eight distinct sections (Figure 18). To achieve this, seven rubber ribs were attached to the concrete surface, directing the leaking water into eight Thomson weirs. These weirs allowed continuous measurement of leakage from each section, providing precise and reliable data for further analysis.

Figure 18. Rubber ribs for sectioning of seepage water during downstream support fill. The flow measured with Thomson weirs (Bernstone et al., 2021).

Figure 19 presents the reservoir water level, turbidity, average water temperature, and leaking rate over the entire measurement period (Hansson et al., 2024).

a   b
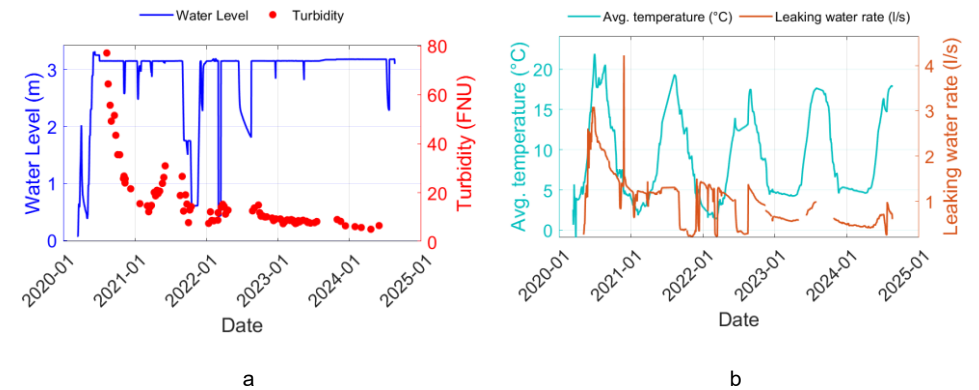
Figure 19. Variations in (a) reservoir water level and turbidity, and (b) average water temperature and leakage rate during the entire measurement period.

To observe changes in pore pressure over time, twelve vibrating wire piezometers were installed throughout the embankment dam structure (see Figure 20). Of these, eight sensors (P3, P4, and P7–P12) were embedded within the dam's core, three (P2, P5, and P6) were placed in the fine filter layer, and one (P1) in the coarse filter. All piezometers were concentrated within a single cross-section located near the dam's right abutment—an area selected for its structural relevance and its potential to reflect characteristic pore pressure trends and seepage conditions within the dam body. The pore pressure values recorded by piezometers from March 2020 to February 2022 are presented in Figure 21.

Figure 20. Cross-section with the location of the vibrating wire piezometers (Bernstone et al., 2021; Lagerlund et al., 2022).

Figure 21. The measured pore pressure values by vibrating wire piezometers (Toromanovic, 2024).

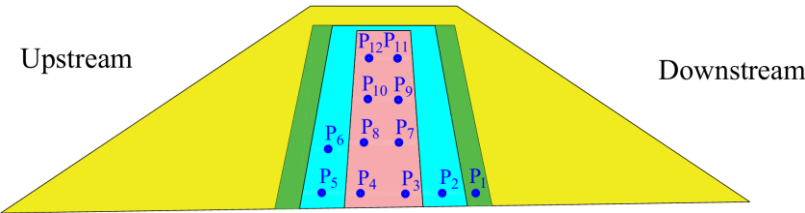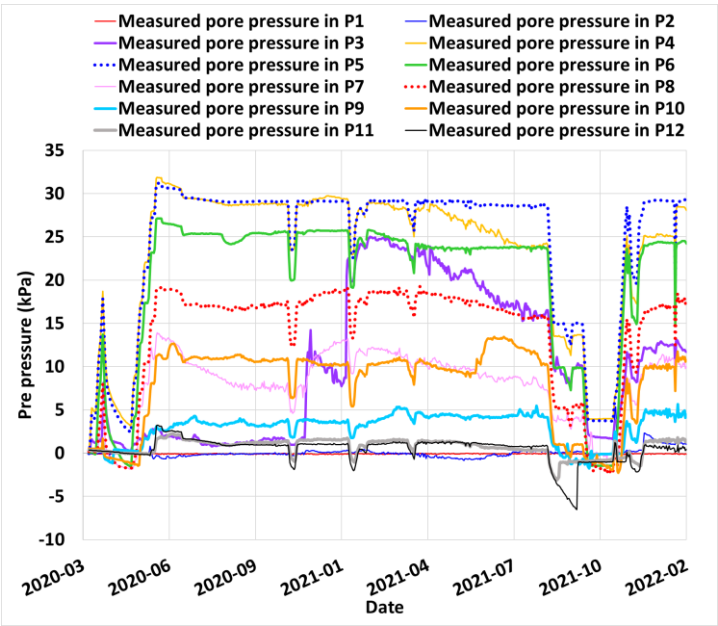The material properties and particle size distribution (PSD) curves, based on the tests conducted by the supplier (Jehander) and Luleå University of Technology (LTU), are presented in Table 2 and Figure 22 respectively. The PSD for the core and fine filter materials is based on testing conducted at LTU after construction, using samples from the delivered material. In contrast, the PSD for the coarse filter and support fill materials corresponds to the specifications of the ordered material from Jehander. Notably, discrepancies were observed between the ordered and delivered materials for the core and fine filter.

Additionally, hydraulic conductivity measurements were carried out by VRD and LTU on compacted soil samples, with the results summarized in Table 3. At VRD, tests were performed on five core samples with a water content ranging from 6–10% and a consistent degree of compaction (Bernstone et al., 2021). At LTU, four soil samples were tested using the falling head permeameter method. The results revealed that the hydraulic conductivity of the core material was approximately ten times higher when tested with this method compared to VRD's triaxial permeability cell. For the fine filter, coarse filter, and support fill, test results from large-scale permeameter experiments are also reported in Table 3.

Table 2. Estimated material characteristics based on initial laboratory analysis (Lagerlund et al., 2022).

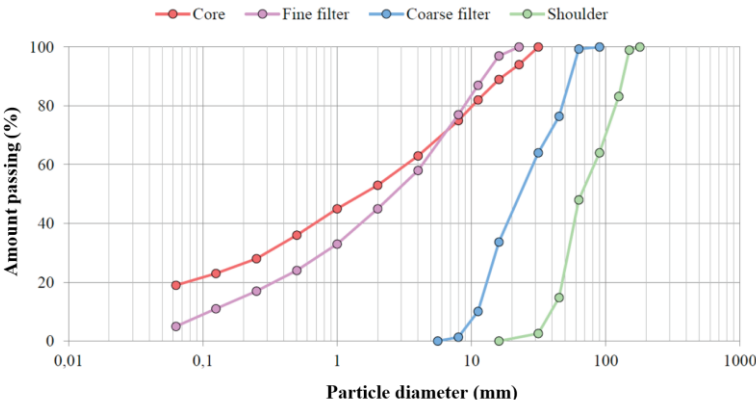| Property	Core (Moraine, 0–20 mm)	Fine Filter (Crushed Rock, 0–16 mm)	Coarse Filter (Crushed Rock, 8–64 mm)	Structural Fill (Crushed Rock, 32–154 mm)
Hydraulic Conductivity (m/s)	$\sim 1 \times 10^{-7}$	$\sim 1 \times 10^{-5}$	$\sim 1 \times 10^{-2}$	$\sim 1 \times 10^{-1}$
Dry Density (t/m³)	2.25	1.9	1.7	1.8
Internal Friction Angle	42°	36°	40°	41°

Figure 22. PSD graphs based on the tests conducted by Jehander and LTU (Bernstone et al., 2021).

Table 3. Results from permeameter tests of the material at VRD and LTU (Bernstone et al., 2021).

Permeameter	Material	Hydraulic conductivity (m/s)	Carried out by:
Triaxial permeameter cell 1	Core	5.99×10^{-9}	VRD
Triaxial permeameter cell 2	Core	3.74×10^{-10}	VRD
Triaxial permeameter cell 3	Core	8.41×10^{-10}	VRD
Triaxial permeameter cell 4	Core	1.92×10^{-10}	VRD
Triaxial permeameter cell 5	Core	4.64×10^{-10}	VRD
Falling head permeameter 1	Core	5.15×10^{-8}	LTU
Falling head permeameter 2	Core	3.11×10^{-8}	LTU
Falling head permeameter 3	Core	9.18×10^{-8}	LTU
Falling head permeameter 4	Core	3.82×10^{-8}	LTU
large-scale permeameter	Fine filter	5.60×10^{-5}	VRD
large-scale permeameter	Coarse filter	2.70×10^{-1}	VRD
large-scale permeameter	Structural fill	4.50×10^{-1}	VRD

4.4 Geophysical measurements

A total of 224 electrodes were embedded within the test embankment to carry out ERT and IP measurements. The 3D configuration of the electrode arrays is illustrated in Figure 23. These electrodes were constructed from stainless steel plates measuring 80 mm by 80 mm, fabricated using 0.5 mm acid-resistant stainless steel. Figure 24 shows the electrode arrangement on the dam crest, where the steel plates are integrated into measurement lines alongside seismic cables and plastic tubes that house additional equipment. According to modelling results in (Rücker & Günther, 2011), the electrode plates were small enough to be approximated as point sources with a modelling error below 1%.

Six horizontal electrode lines, each comprising 32 electrodes with a planned spacing of 61–63 cm, were buried at strategic levels: one line on top of the clay core and two levels within the adjacent filters—at the bottom and midpoint heights (the pink, yellow, and red horizontal lines in Figure 23). Additionally, four near-vertical arrays were positioned at each end of the dam within the filter zones, each consisting of 8 electrodes spaced 50 cm apart vertically (the blue and green vertical lines in Figure 23). However, because the geoelectrical installation team was not present during the construction, the actual placement of electrodes deviated significantly from the planned uniform spacing. This irregularity impacted the generation of the FE mesh used for modelling, as discussed later.
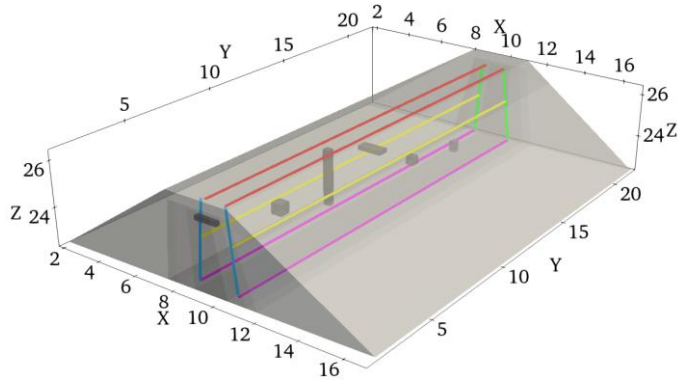
Figure 23. Configuration of the measurement lines (Norooz et al., 2024). The pink lines indicate the horisontal measurement lines at the bottom, the yellow lines represent the horisontal measurement lines at mid-height of the core, and the red lines show the horisontal measurement lines at the top of the core. The blue and green lines indicate the vertical measurement lines at the abutments.
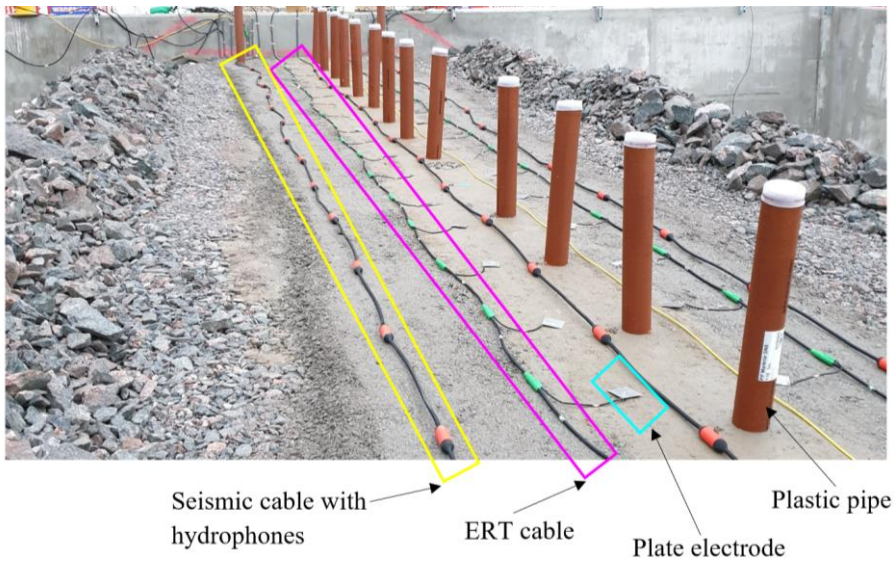
Figure 24. Installation of stainless-steel electrodes along the dam crest, with visible plastic pipes used for seismic sources. Photo by Jasmina Toromanovic (Norooz et al., 2024).

A fully automated data acquisition system was set up to collect and transmit ERT and IP data daily. This system includes an ABEM Terrameter LS2, a custom-built relay switch with lightning protection, an industrial PC, and a network router (see Figure 25). The relay enables selection of 2 sets of 32 electrodes at a time from a

total of 8 lines. The data acquisition and transfer routines are controlled via Python scripts running on the PC.

To enhance spatial resolution and defect detectability, various array configurations were applied, including bipole-bipole (Bing & Greenhalgh, 2000), multiple gradient (Dahlin & Zhou, 2006), extended gradient (Zhou et al., 2020), and corner arrays (Tejero-Andrade et al., 2015). These configurations were chosen to ensure that data points covered the entire core volume and that the zoned design of the dam was respected. The electrode profiles were strategically located close to the core to improve detection depth, as surface-only layouts would have limited subsurface resolution. Crossline measurements connecting horizontal arrays at different heights were used to enhance data coverage in the central core region. Inclined profiles near both abutments improved coverage at the dam abutments, and corner arrays between inclined and horizontal lines targeted the upstream and downstream boundaries of both the core and fine filter zones. Additional data collection was achieved using extended gradient arrays on each horizontal line.

Initially, the system gathered approximately 7 500 data points per day. This was later increased to about 14 000 daily readings by integrating asymmetric and non-standard electrode pairings, thereby expanding the input for the inverse modelling phase.

Electrode contact resistance, measured using the focus-one technique (Ingeman-Nielsen et al., 2016), ranged from several hundred to a few thousand ohms. Table 4 presents statistical data on the resistance values for each layout, including averages, minimums, maximums, and standard deviations across the full monitoring period. The results indicate that the electrode resistances remained within acceptable and manageable levels.

Table 4. Summary statistics of electrode contact resistance for each layout during the monitoring campaign (Norooz et al., 2024).

Layout	Mean Rc (Ω)	Min Rc (Ω)	Max Rc (Ω)	Std. Dev. (Ω)
Crest Upstream	1022	727	1442	121
Crest Downstream	1840	1078	3056	273
Mid Upstream	1456	671	2480	255
Mid Downstream	1615	933	2473	224
Bottom Upstream	1333	764	1824	179
Bottom Downstream	1861	567	2672	525
Ends Layout	2492	1611	3467	350
Total	1659	567	3467	528

Relay switch with transient protection ⟹

Industry PC & network router ⟹

ERT / DCIP instrument ⟹

Power supply ⟹

Figure 25. Geophysical monitoring setup at the Älvkarleby test facility (Norooz et al., 2024).

5 Results and discussion

This chapter begins by presenting the synthetic modelling results obtained prior to the field measurements. It then presents the reciprocal error calculated for both the field ERT and IP data in order to evaluate data quality, followed by the results of the filtering procedures applied to enhance measurement reliability. Subsequently, the internal defects identified through ERT and IP analyses are presented and discussed. The chapter then continues with the results of the seepage modelling and concludes with an examination of how integrating ERT data with seepage modelling can improve the overall accuracy and reliability of the findings.

5.1   Synthetic modelling

Prior to the commencement of field measurements, a comprehensive 3D synthetic model was developed to evaluate and optimize various electrode configurations and measurement combinations. Its geometry reflects the planned dimensions of the actual test dam (Figure 26a) (Norooz et al., 2021).

The electrical properties of the dam materials were defined based on laboratory measurements, with the clay core assigned a low resistivity (~21 $\Omega \cdot m$) in contrast to the significantly higher resistivity values of the surrounding filters and rockfill zones (ranging from hundreds to several thousand $\Omega \cdot m$) (Table 5). To simulate potential seepage pathways or internal erosion zones, five small anomalies—representing voids or high-resistivity inclusions with dimensions between 0.1 and 1.3 m—were embedded within the core material (see Figure 26b and Table 6).
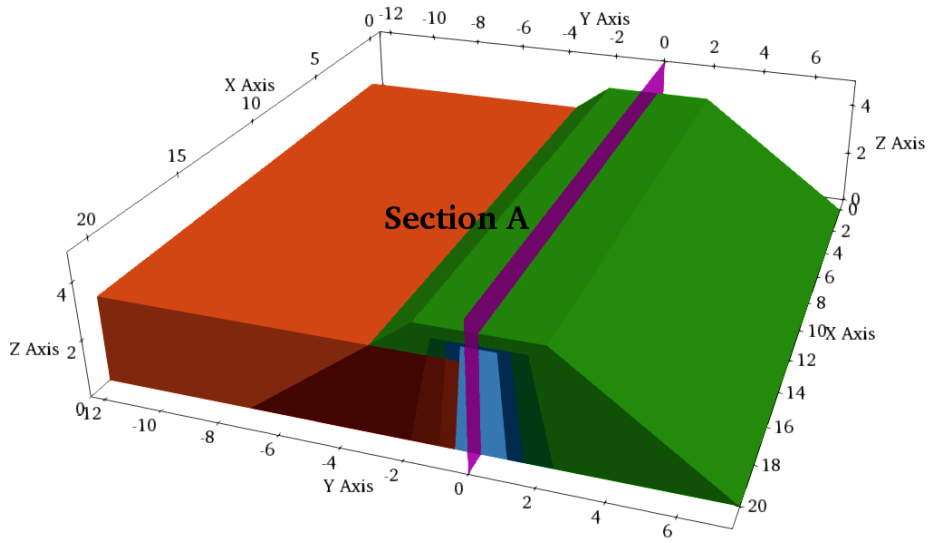
a
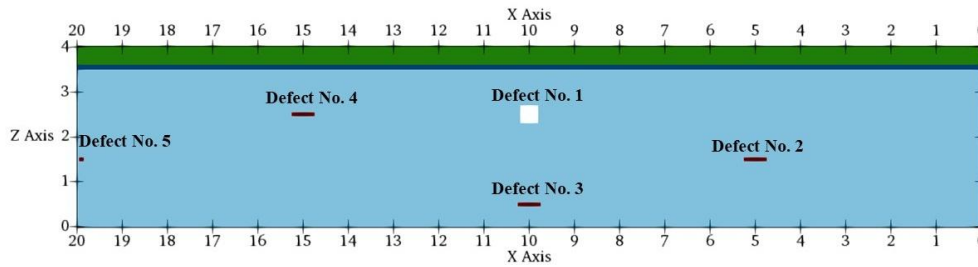
b

Figure 26. Position of defects in the core; a) Position of cross-section planes of A; b) Section A and the position of defects in the core (Norooz et al., 2021).

Table 5. Material resistivity used in the forward modelling (Norooz et al., 2021).

Region	Resistivity (Ω.m)	Material Marker
Reservoir	240	10
Core	21	1
Fine filter (above water)	1000	2
Coarse filter (above water)	2000	3
Fine filter (below water)	180	12
Coarse filter (below water)	500	13
Rock fill (above water)	20000	4
Rock fill (below water)	1500	14

Table 6. Simulated defects placed in the clay core. Defect No. 1 was considered to be a hole in the clay core (Norooz et al., 2021).

Defect No.	Shape	Size			Coordinate of the centre point	Resistivity (Ω.m)
		Δx	Δy	Δz		
1	Cube	0.4 m	0.4 m	0.4 m	(10,0,2.5)	Infinitely resistive
2	Cuboid	0.5 m	1.3 m	0.1 m	(5,0,1.5)	180
3	Cuboid	0.5 m	1.4 m	0.1 m	(10,0,0.5)	180
4	Cuboid	0.5 m	1.2 m	0.1 m	(15,0,2.5)	180
5	Cuboid	0.1 m	1.3 m	0.1 m	(19.9,0,1.5)	180

A variety of ERT measurement arrays were simulated to maximize sensitivity to core heterogeneities. In particular:

Extended gradient arrays were applied along each horizontal line, generating 3636 data points by injecting current between electrodes in the same line and measuring potentials at offset positions. This array provides high signal-to-noise ratio and dense core coverage, extending to upstream/downstream borders of the core.

Cross-line bipole–bipole arrays (Bing & Greenhalgh, 2000) connected electrodes between adjacent horizontal profiles. Two cross-line configurations were modelled: one linking electrodes at the same elevation on neighbouring lines (3 combinations, 1227 points) and another linking different elevations (8 combinations, 2454 points). These 3681 measurements probe resistivity contrasts across the dam's width.

Corner arrays (Tejero-Andrade et al., 2015) were placed at the junctions of inclined (filter) and horizontal (core) lines. With 224 data points, these focus on deep or edge anomalies near the upstream/downstream faces.

Vertical (end) bipole–bipole arrays between inclined end-lines (4 combinations, 148 points) further enhance end-of-core sensitivity.

In total, about 7941 apparent-resistivity measurements were generated across the survey. A refined tetrahedral mesh ($\sim 2\times 10^{\wedge}6$ cells, quality q≈1.2) was used for FE forward modelling (Figure 27).
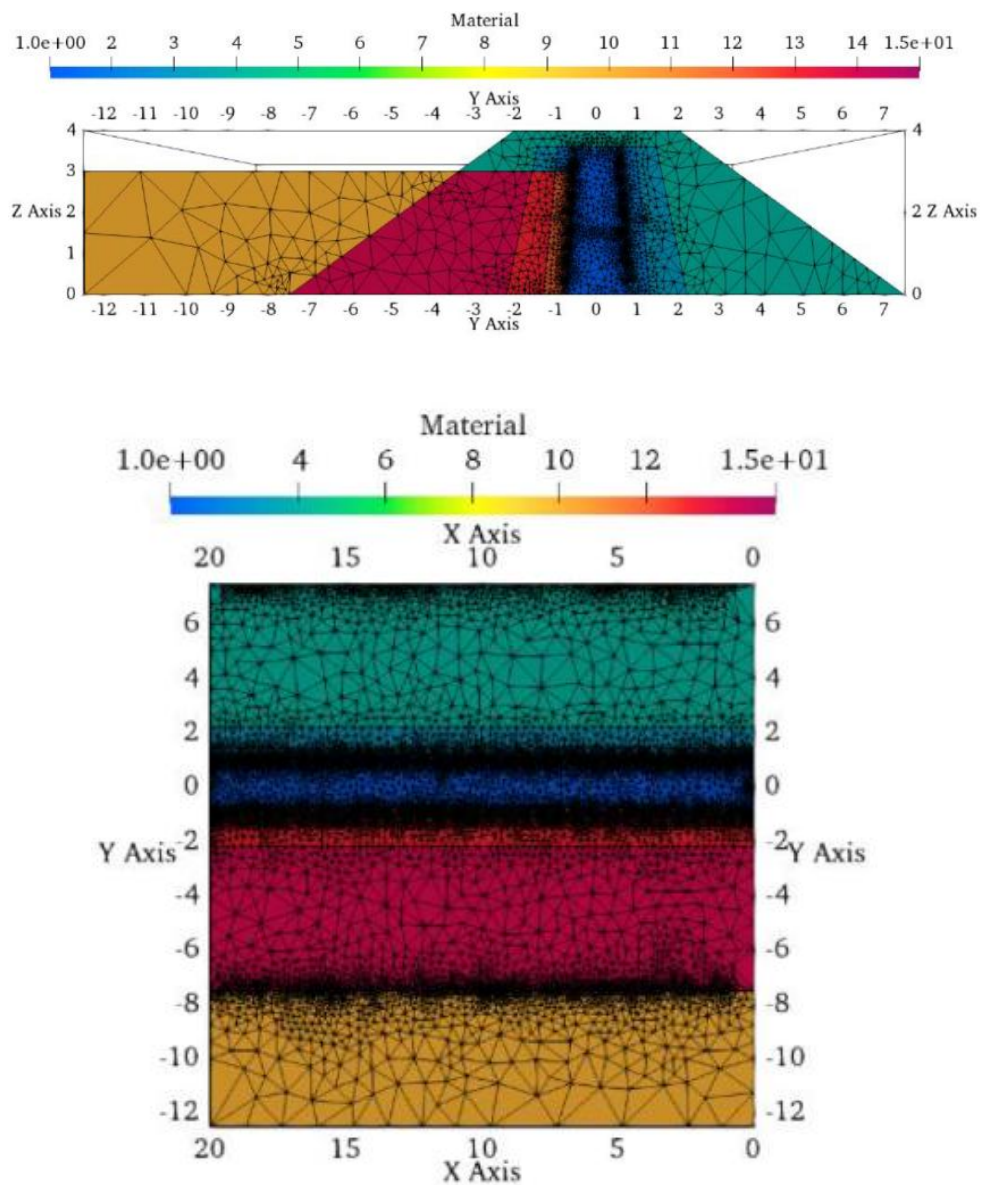
Figure 27. Medium mesh with around 2,000,000 cells, quality of 1.2 and quadratic shape function used in the forward modelling.

The full synthetic dataset was inverted simultaneously in 3D using both L1 (robust) and L2 (least-squares) norm regularization, with and without a priori region constraints. Unconstrained inversions (i.e. no structural prior) produced generally poor models. The L1-norm inversion without constraints yielded spurious resistive anomalies (e.g. artificial resistive zones at the top/bottom of the core) and did not reliably image the defects (Figure 28). The five core defects remained indistinct amid inversion artifacts: defects near each other were "smeared out" and the void (Defect 1) did not emerge clearly. In short, unconstrained inversions suffered from strong 3D ambiguity, yielding unrealistic resistivity distributions and missing the seepage indicators.

In the following, the inversion results of the models containing the prior information are presented. The inversion results in the clay core were extracted from the model to investigate the defect positions. The results are shown from both sides of the core as explained in Figure 29 (view 1 and 2). In addition, four cross-sections in the defect location in the core were taken out to assess the capability of the models in predicting the defect locations (Figure 29).

When realistic region-based constraints were applied (using prior resistivity ranges for core, filters, rockfill, etc. presented in Table 7), the inversion results improved dramatically (Figure 30). The most effective constraint scheme (R3: moderately narrow resistivity bounds around laboratory values) allowed both L1 and L2 inversions to recover the defect geometry. In the constrained L1-norm solution, each discrete defect emerged as a distinct high-contrast zone in the core cross-section (Figure 30a). In the constrained L2-norm solution, the anomalies were also detected and the surrounding gradients were smoother (Figure 30b). Notably, L1 best located isolated defects while L2 more clearly resolved the cluster of closely spaced defects (Figure 30).
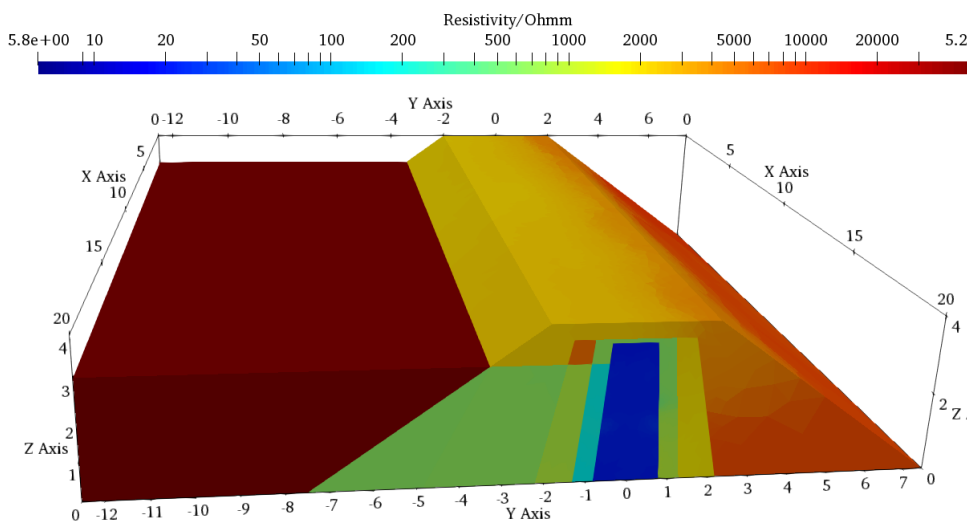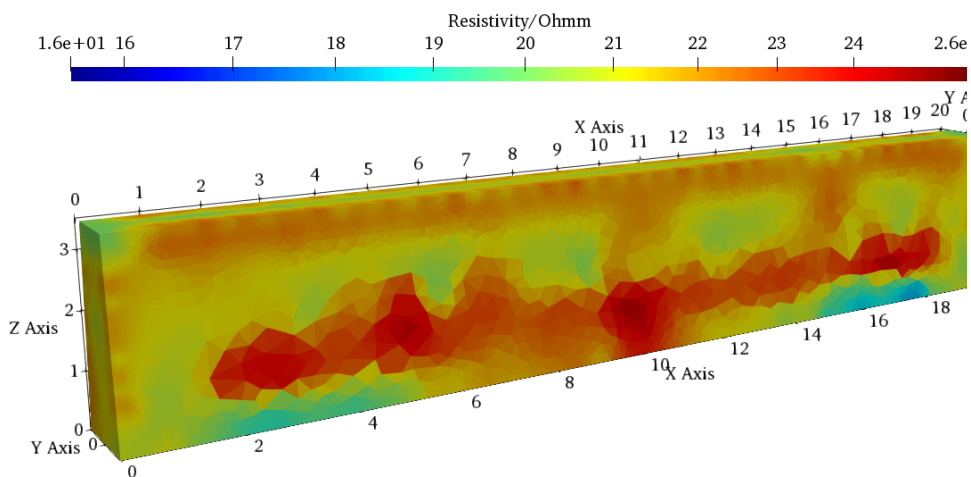
Figure 28. L1 norm Inversion results for model containing 5 defects in the clay core without region control. a) L1 norm inversion results of whole model. b) Inversion results of the core in L1 norm model (Norooz et al., 2021).
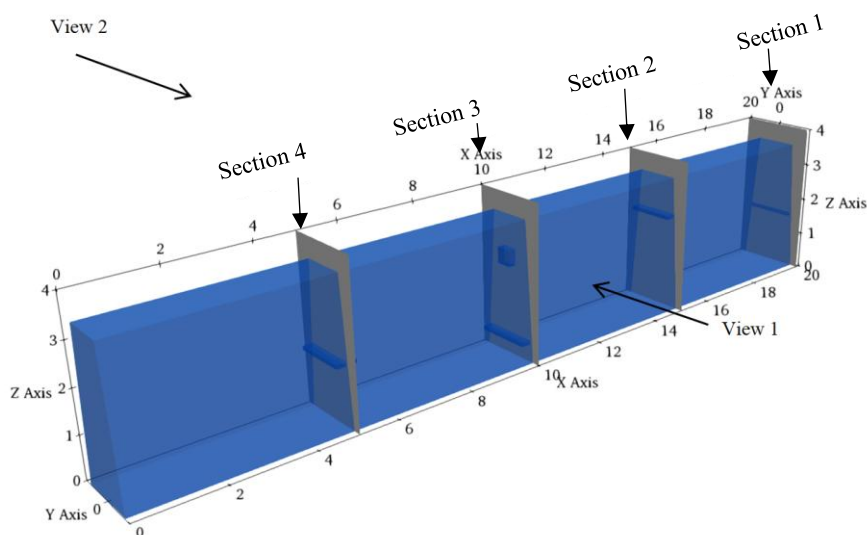
Figure 29. The cross-sections used in the defect locations.

Table 7. Start value, lower and upper bounds for the region controls with broad boundaries used in the inversions (R1 to R4). Note that only the results for region control 3 are shown in this summary.

Material Marker	Region	Start value				Lower bounds				Upper bounds			
		R1	R2	R3	R4	R1	R2	R3	R4	R1	R2	R3	R4
1	Core	21	60	21	21	12.6				200	200	20000	29
2	Fine filter (above water)	1000				600				1400			
3	Coarse filter (above water)	2000				1200				2800			
12	Fine filter (below water)	180				108				252			
13	Coarse filter (below water)	500				300				700			
4	Rock fill (above water)	20000				12000				28000			
14	Rock fill (below water)	1500				1500				2100			
10	Water	240				144				336			

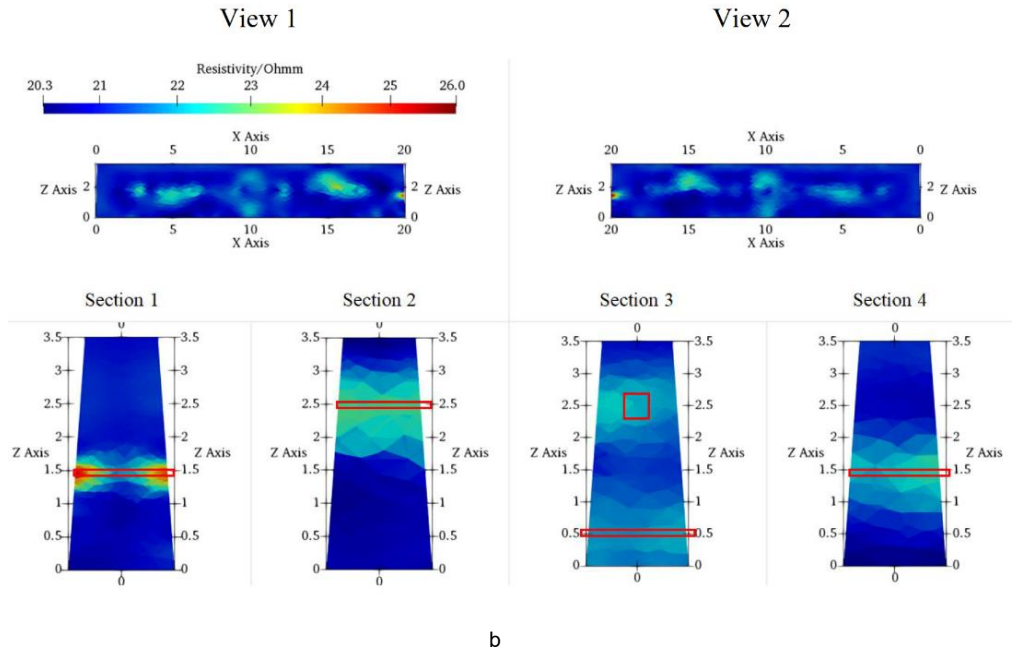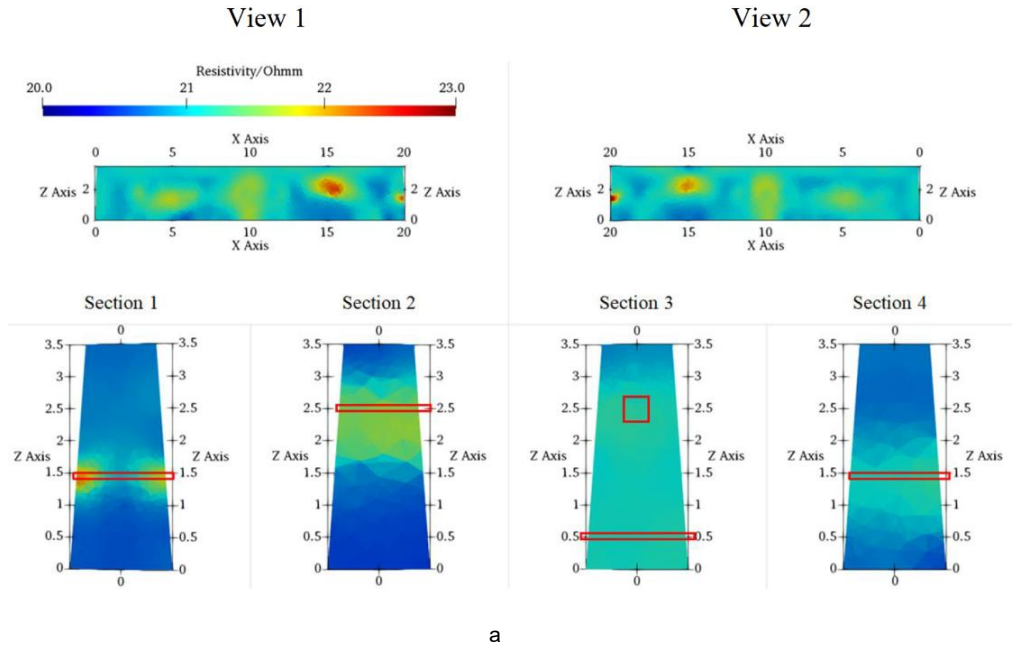**Figure 30.** The inversion results of the clay core for model containing 5 defects in the clay core with region control 3. a) Blocky model option with Narrow boundaries. b) L2 norm model option with Narrow boundaries (Norooz et al., 2021).

5.2 Reciprocal error values for ERT and IP

The reciprocal error values show that most resistivity measurements have relatively low errors, generally below 2%, particularly during the early monitoring phase (2020–2021) (Figure 31a). This suggests a stable and high-quality dataset during this initial period. However, starting in mid-2022, a broader range of error values is observed, including occasional spikes above 5%.

Similarly, for the IP data, reciprocal errors remained low—typically less than 10 ms—during the early monitoring phase (2020–2021), suggesting consistent and reliable measurements (Figure 31b). Starting around mid-2022, both the frequency and magnitude of higher error values increase noticeably, with some measurements surpassing 70 ms.

These trends may reflect alterations in instrumentation, environmental influences (e.g., varying moisture or temperature conditions), or a rise in ambient electrical noise affecting data quality.
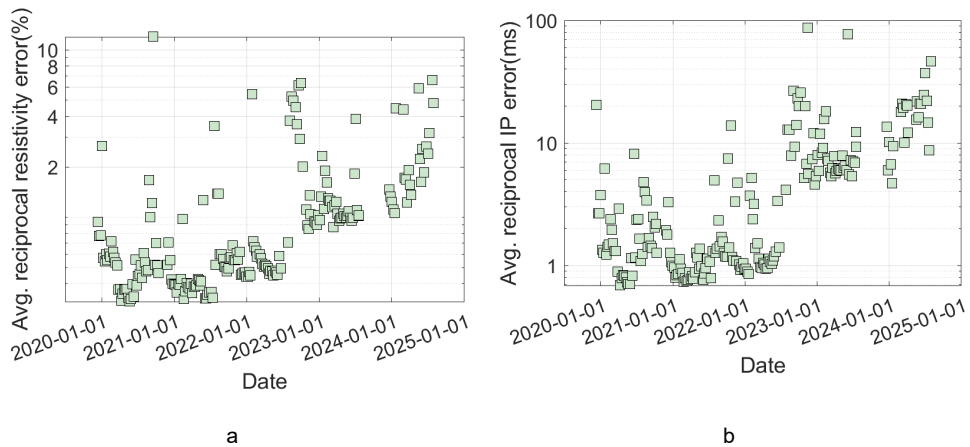
Figure 31. Average reciprocal error for resistivity (a) and IP data (b) during the whole period of the measurements.

As an example, Figure 32 presents the reciprocal errors for four selected electrode combinations. Overall, the resistivity data exhibit relatively low error levels, with the majority of measurements showing reciprocal errors below 7%. Only a small number of data points exceed this threshold (Figure 32a). For the IP data (Figure 32 b), most reciprocal error values remain below 10 ms, suggesting an overall acceptable quality of the dataset throughout the monitoring period.
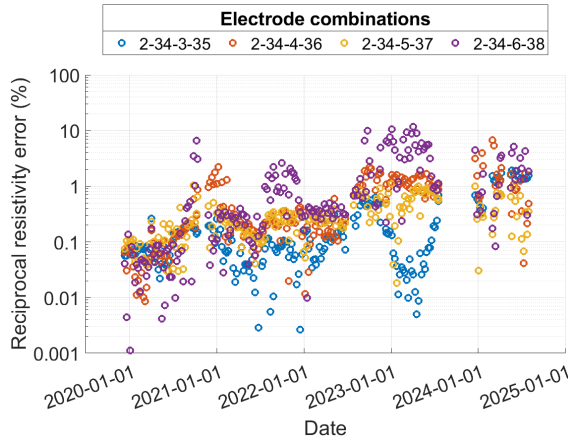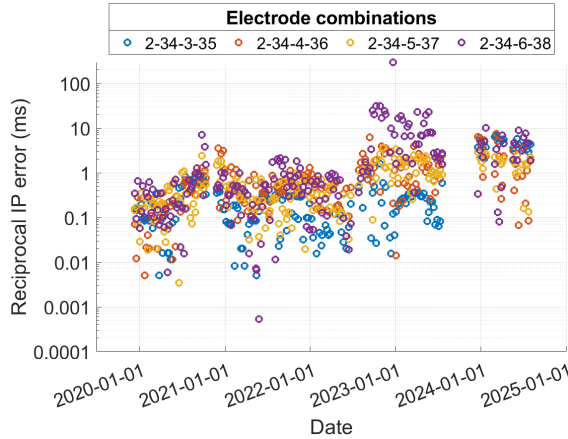
Figure 32. Reciprocal error for resistivity (a) and IP (b) data throughout the entire measurement period for four selected electrode combinations.

5.3 Filtering ERT/IP data results

To ensure the quality and reliability of the dataset prior to inversion, a comprehensive temporal filtering and outlier detection procedure was applied. Figure 33a shows the average and median resistivity values over time, where only a few outliers are apparent. This finding, consistent with the low reciprocal errors observed in the ERT data, indicates generally higher data quality and stability in the resistivity measurements. In contrast, Figure 33b illustrates the temporal evolution

of the average and median chargeability values, which exhibit several pronounced outliers, many of which are highlighted with blue bounding boxes.

a

b
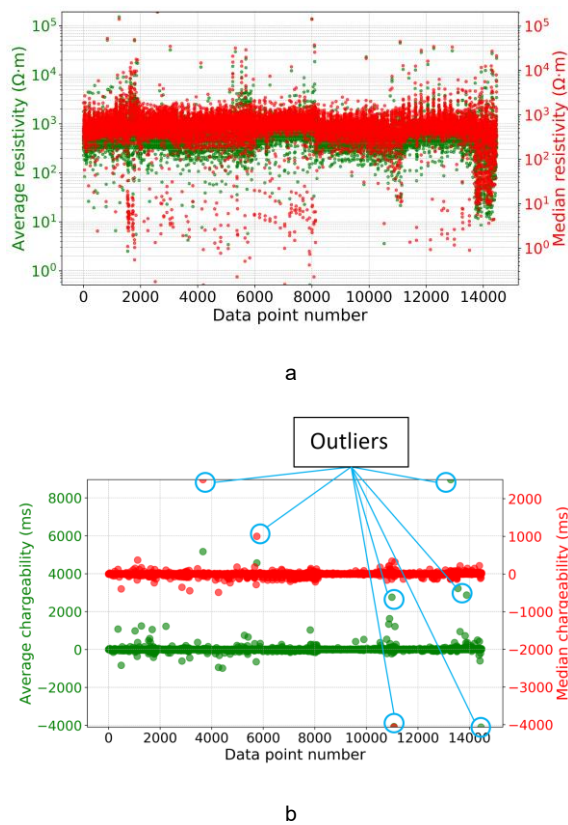
Figure 33. The average and median of the resistivity (a) and chargeability (b) values for the data points collected during the measurement period.

A more detailed example is presented in Figure 34a and Figure 35a, which shows the raw resistivity and chargeability time-series for data points 4620 to 4629. Notably, some data points display abrupt spikes, while some series are relatively smooth. These spikes underscore the importance of a robust filtering process capable of handling both gradual trends and transient disturbances. To tackle these issues, two different filtering methods were applied, and the results are presented in Figure 34 and Figure 35.

The results of the bidirectional IIR low-pass filter (Method 1) are presented in Figure 34b and Figure 35b. Method 1 effectively reduces the spike magnitudes observed in Figure 34a and Figure 35a.

The results of the low-pass filtering method with pre-smoothing (Method 2) are shown in Figure 34c and Figure 35c, clearly demonstrating that the method effectively removes spikes and significantly smooths local fluctuations.

Data point 4621 shows a pronounced spike in both resistivity and chargeability in May 2023, which is effectively removed by Method 2 (Figure 34c and Figure 35c). In addition, several data points exhibit a short-term increase in resistivity during February–March 2022 (Figure 34a). This anomaly is also mitigated by Method 2 (Figure 34c).

Method 2 (Figure 35c) proved more effective in removing extreme outliers from the chargeability data, whereas Method 1 (Figure 35b) only managed to partially reduce the amplitude of these anomalies.

The reciprocal errors for ERT and IP data, after applying filtering Method 2, are presented in Figure 36. Compared to the reciprocal errors before applying the filtering (Figure 31), it is evident that the filtering significantly reduced the errors. Prior to filtering, the maximum average reciprocal error for the resistivity data was approximately 11% (Figure 31a), whereas after filtering it decreased to around 3.5% (Figure 36a).

For the IP data, the improvement is even more pronounced. Before filtering, the maximum reciprocal error was around 100 ms (Figure 31b), but after applying the filter, the maximum average error decreased substantially to approximately 3 ms (Figure 36b).
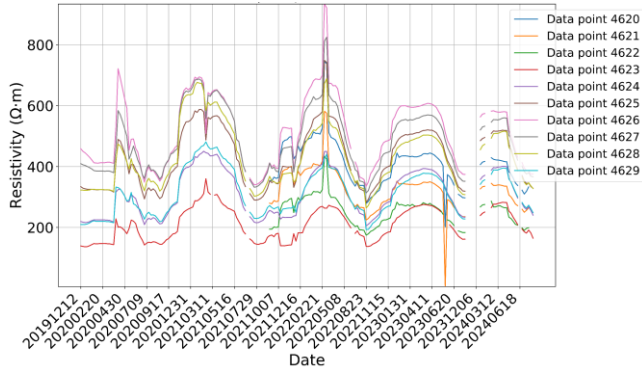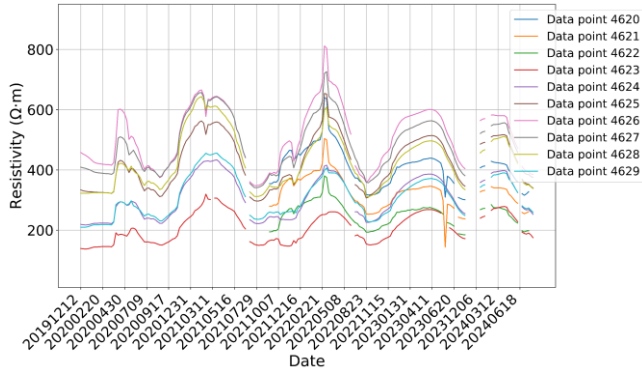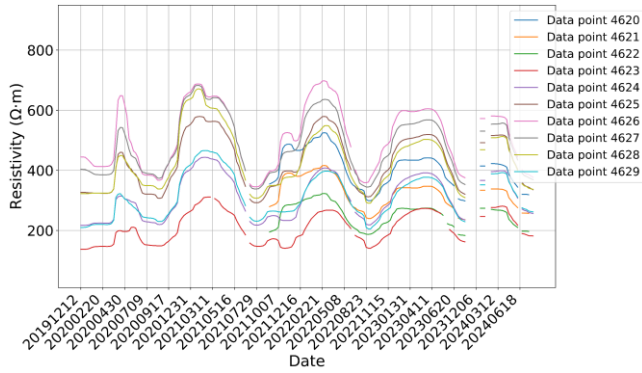
Figure 34. (a) Raw resistivity data for measurement points 4620 to 4629 over the full duration of the acquisition. (b) Filtered resistivity using the bidirectional IIR low-pass filter. (c) Filtered resistivity using the low-pass filtering method with pre-smoothing.
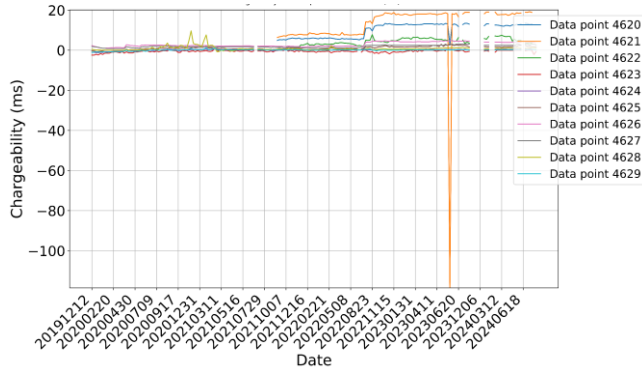
a
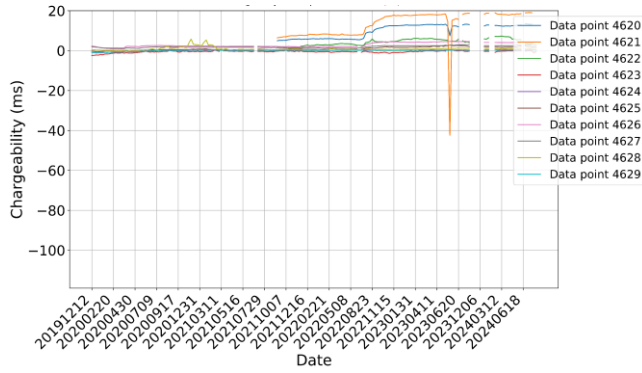
b
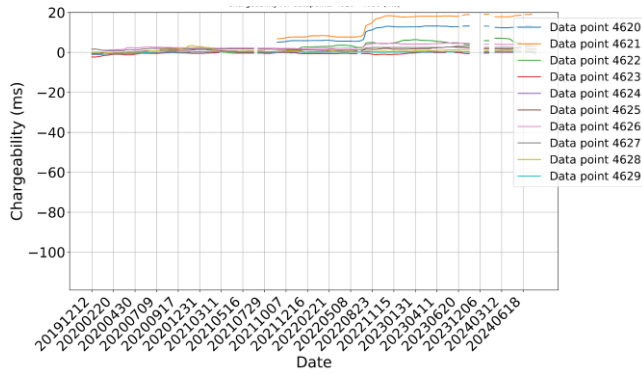
c

Figure 35. (a) Raw chargeability data for measurement points 4620 to 4629 over the full duration of the acquisition. (b) Filtered chargeability using the bidirectional IIR low-pass filter. (c) Filtered chargeability using the low-pass filtering method with pre-smoothing.

Figure 36. Average reciprocal error for resistivity (a) and IP data (b) over the entire measurement period, following the application of filtering Method 2.

5.4 Detection of intentional defects

This section presents the inversion outcomes for both the core and the upstream fine filter. These parts were extracted from the overall dam structure to enable a focused assessment of the inversion performance in regions previously identified as containing certain defects (see Figure 37).

Figure 37. Extracted sections of the dam body used for analysis: the core zone and the upstream fine filter. These areas were selected to evaluate inversion results in regions known to contain structural defects.

Figure 38 presents the average inverted resistivity values for the core and the upstream fine filter, covering the full 4.5-year monitoring period. Elevated resistivity values are visible in the areas surrounding Defects No. 2 and 3 within the core (Figure 38a, b). According to (Norooz et al., 2024), these anomalies were already detectable during the early stages of dam operation, confirming that the defects could be reliably identified both at the initial stage and in the averaged data over 4.5 years. This consistency highlights that Defects No. 2 and 3 were among the most clearly identifiable using ERT.

An area of increased resistivity is also observed near Defect No. 4 (Figure 38a, b). According to (Norooz et al., 2024), this anomaly was already detectable in the initial measurements. This suggests that it may be associated with the washout of fine material around the concrete block defect (Defect No. 4), which was detectable both at the early stage of dam operation and in the averaged data over the 4.5-year monitoring period.

Defect No. 1 was not detected in the early stage, possibly due to the high-water absorption capacity and electrical conductivity of wood, which reduce resistivity contrast with surrounding materials (Norooz et al., 2024). However, in February 2024, high-resistivity anomalies emerged around the location of this defect, visible from the upstream side (Figure 38a). These anomalies appear linked to fine-material washout and increased seepage in the area. After dam removal, extensive internal erosion surrounding Defect No. 1 was confirmed (Lagerlund, 2025).

Defect No. 5 remained undetected, potentially because of its small size and distal location within the core, where data coverage is reduced near the abutments (Figure 38a, b) (Norooz et al., 2024).

Furthermore, additional high-resistivity zones were identified, and post-removal inspections confirmed that internal erosion had occurred in several parts of the structure (Lagerlund, 2025). In particular, vertical Defect No. 3 indicates that internal erosion progressed from the bottom of the core beneath Defect No. 3, as well as through the defect itself, extending from the upstream to the downstream side. This interpretation is supported by the elevated resistivity values observed along the entire vertical extent of the defect (black dashed box in Figure 38a, b).

Another extensive area of the core, between x = 16 and 21 m, was found to be affected by internal erosion following dam removal (Lagerlund, 2025). It is likely that the internal erosion had extended through both the core and the fine filter; however, post-removal inspections did not focus on the fine filter, and no observations regarding it were reported. This area was identified through resistivity measurements, as indicated by the black dashed bounding box at the bottom of the core and the upstream fine filter, around x = 16–21 m Figure 38 a-c.

An area of eroded core material was discovered around at the right abutment after the dam was removed (Lagerlund, 2025). This erosion had not been detected by the ERT survey, which may be due to the lower data coverage near the dam abutment.

Another area at the bottom of the core, around x = 3 m, was identified through high resistivity measurements (black dashed bounding box Figure 38a, b). This area

may correspond to eroded core material that was not observed during the dam removal, possibly due to lack of details in the inspections conducted at that time.

A layered resistivity structure is also visible in the core, characterized by a sequence of higher, lower, and higher resistivity values from top to bottom. This pattern may be associated with variations in soil moisture content, differences in soil compaction, or other stratigraphic factors (Figure 38a, b) (Norooz et al., 2024).

As mentioned earlier, in November 2022, an injection process using magnetite-containing materials was carried out in two of the boreholes. However, none of these injections were detected in the ERT measurements (Figure 38a, b). Most of the anomalies observed at the bottom of the core were already present prior to the injections according Norooz et al. (2024), indicating that these areas are not associated with the accumulation of injection material.

Figure 39 shows the minimum chargeability values derived from the low-pass filtering method with pre-smoothing IP data. Low values are observed around Defects No. 2 and 3, which were previously identified as high-resistivity zones (Figure 38a, b).

Defect No. 4, previously identified based on high resistivity measurements, also exhibits slightly reduced chargeability in its surrounding area; however, this signal is not sufficiently distinct to confirm the defect solely from the IP data. The resistivity model proved more effective for identifying this feature (Figure 38 and Figure 39).

As noted earlier, Defect No. 1 was not detectable during the initial phase of dam operation. Following February 2024, however, high-resistivity anomalies were recorded near this defect, particularly on the upstream side (Figure 38a). In the IP model, the same location appears as a zone of low chargeability (Figure 39a). Post-removal documentation confirmed extensive internal erosion in this area (Lagerlund, 2025).

Defect No. 5 could not be identified in either the resistivity or IP models (Figure 38a, b and Figure 39). After the dam demolition, some areas affected by eroded material were detected around this defect; however, the DCIP data could not detect them due to the lack of data coverage near the abutments.

Several regions identified by high resistivity also correspond to low-chargeability zones in the IP model, notably those marked by black dashed boxes at the base of the core (Figure 38a, b and Figure 39).
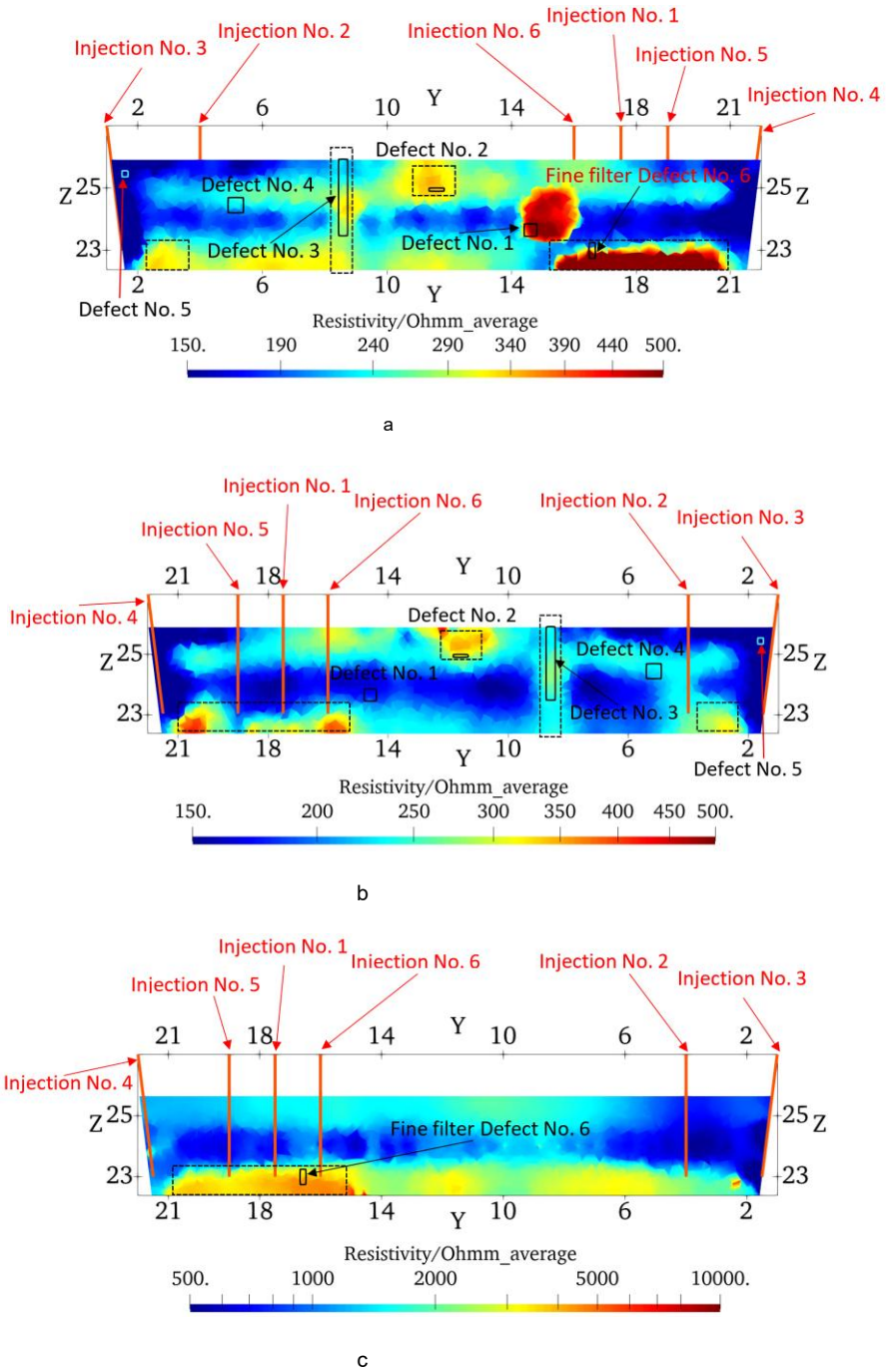
Figure 38. The average inverted resistivity values over the full duration of the acquisition; a) core upnstream side; b) core downstream side; c) upstream fine filter.
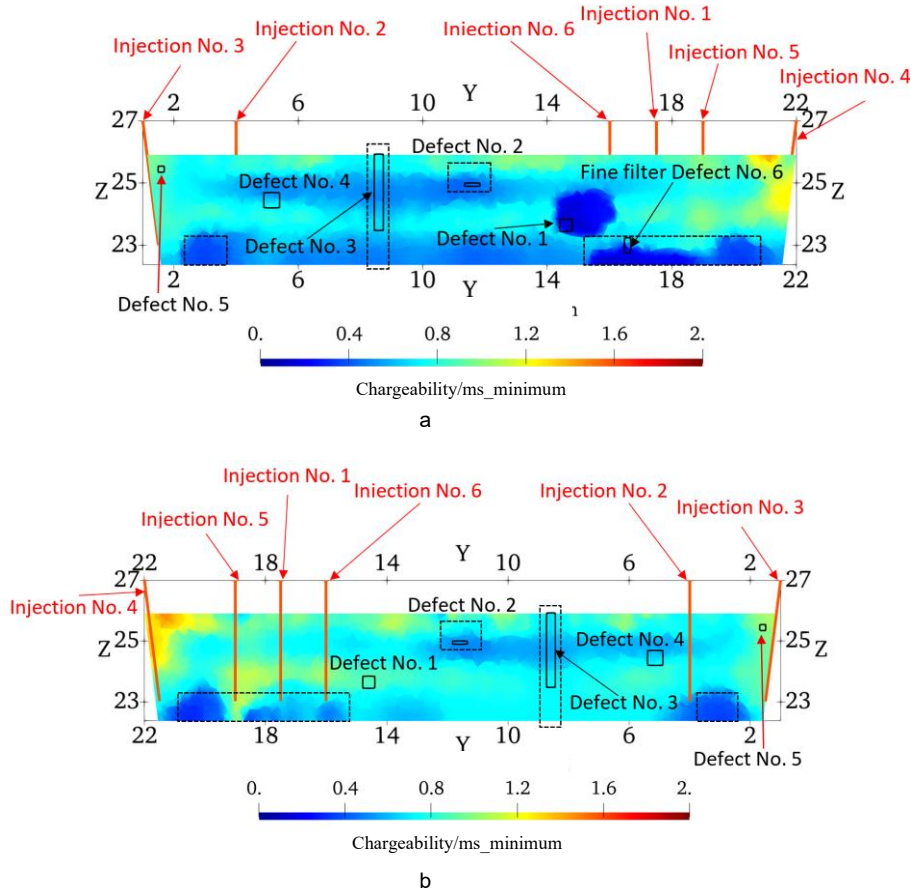
Figure 39. Minimum inverted chargeability values over the full duration of the acquisition, based on unfiltered IP data; (a) filtered IP data (the low-pass filtering method with pre-smoothing) – core upstream, (b) filtered IP data (the low-pass filtering method with pre-smoothing) – core downstream.

5.5 Integration of ERT with seepage modelling

In this study, transient seepage flow was modelled using SEEP3D, a FE module within the GeoStudio software suite. The simulated pore water pressures and seepage rates were compared with daily measurements collected over a period of approximately 1.5 years, from March 2020 to October 2021.

To systematically assess the influence of spatially variable material properties and detected anomalies on seepage behaviour, three seepage models were developed and compared (Figure 40). Model 1 represents an idealized dam body without defects (Figure 40a), while Model 2 incorporates the intentionally

constructed defects (Figure 40b). Model 3 further integrates both the intentional defects and anomalous zones identified through ERT measurements (Figure 40c). This sequence allows for a detailed evaluation of how including geophysical detected anomalies influences the results of seepage simulations.

A key contribution of this study is the novel integration of 3D ERT-derived resistivity patterns into the seepage model. Unlike conventional approaches that rely solely on construction records, design drawings, and point-based inspections, this method incorporates spatially distributed geophysical data to define internal zonation within the dam. This approach enables a more data-driven, spatially continuous characterization of material properties, enhancing the realism and predictive capability of the seepage model. For example, the layered resistivity structure observed in the core (Figure 38a, b) was explicitly implemented in Model 3 (turquoise areas in the core in Figure 40c), allowing for zonation that reflects subsurface heterogeneity.

In addition to the simulated intentional defects, other anomalous areas were identified by the ERT model and incorporated into seepage Model No. 3. These areas are indicated by green rectangles and labelled as "Anomalous area detected by ERT" in Figure 40c. These zones are not detectable through traditional investigation methods and therefore demonstrate the added value of integrating geophysical data into seepage modelling.

The initial hydraulic conductivity values for Seepage Model 3 were derived from interpretations of 3D ERT data (Figure 38a; b) combined with laboratory results (presented in 4.3 Complementary measurements). In contrast, the initial values for Models 1 and 2 were based solely on laboratory measurements. Temporal variations in hydraulic conductivity for the core and fine filter materials were incorporated into all three models to account for observed changes in turbidity, leakage rates, and pore pressure measurements (Figure 19 and Figure 21), even under a constant reservoir water level (Figure 19a).

The hydraulic conductivity of the core and fine filter materials was refined through a trial-and-error approach to achieve the best agreement with measured leakage rates and pore pressures at Cells P4, P6, and P10.

The total measured leakage rates and pore pressures from Cells P4, P6, and P10 were compared with the simulated values from the three models, and the results are presented below. Figure 41 shows the measured and calculated leakage rates alongside the reservoir water level. Model 3 demonstrates strong agreement with the observed leakage rates, whereas Models 1 and 2 show significant discrepancies. This highlights the added value of incorporating 3D geophysical data into seepage modelling.

Defining dam zonation and material properties solely based on construction records, design drawings, and limited laboratory or site investigations proved insufficient to capture the internal complexity of the dam, as indicated by the poor performance of Models 1 and 2. In contrast, Model 3 benefits from spatially

distributed geophysical information, allowing for a more realistic representation of heterogeneities and potential leakage pathways.
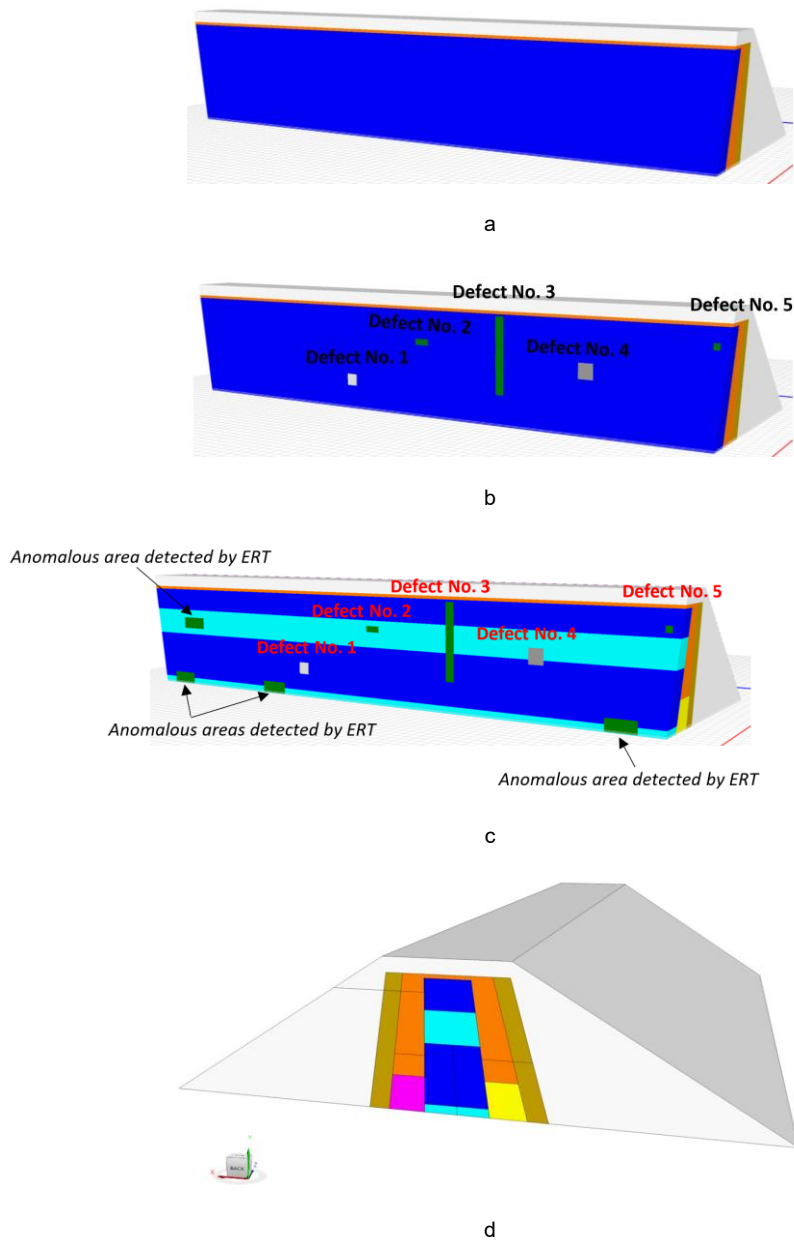

a

b

c

d

Figure 40. Cross-sections through the middle of the core in: a) Model No. 1 with a homogeneous core and fine filter without defects, b) Model No. 2 with a homogeneous core and fine filter containing intentional defects, c) Model No. 3 integrating ERT data and intentional defects, and d) the geometry used in Seepage Model No. 3.

80

Models 1 and 2 predict very low leakage rates, whereas the results from Model 3 are more consistent with actual measurements (Figure 41). The similarity of leakage predictions from Models 1 and 2 likely reflects the small size of the intentional defects, which contribute minimally to overall leakage. This emphasizes that the anomalies detected through ERT are the primary contributors to leakage and must be incorporated into the modelling to accurately reproduce the observed seepage behaviour.
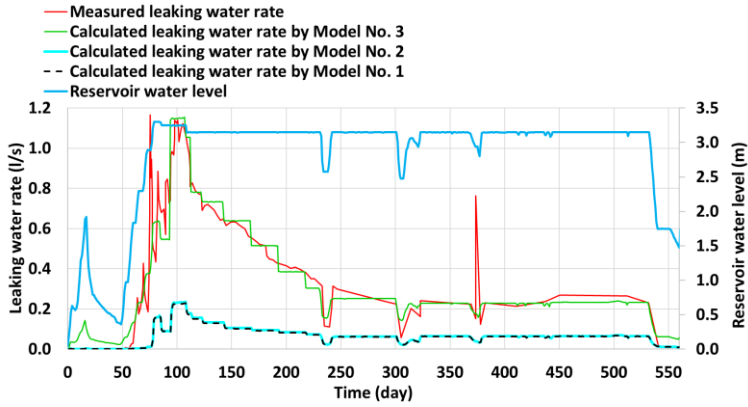

Figure 41. The measured and calculated leaking water rate and the reservoir water level.

The calculated pore pressure at location of Cells P4, P6 and P10 by the models and the corresponding measured pore pressure are presented in Figure 42. Models No. 1 and 2, which rely solely on conventional material property definitions, show similar pore pressure predictions but differ significantly from observations at certain locations. Model No. 3, augmented with ERT-derived resistivity data, provides consistently improved agreement with the measured pore pressures across all three cells.

In Cell P4, Model No. 3 provides a more accurate representation than Models No. 1 and 2. While Models No. 1 and 2 predict a relatively lower pore pressure than the observed measurements (Figure 42a), they fail to capture the decrease in pore water pressure after day 442. Model No. 3, on the other hand, reflects this decline more effectively. Although the observed decrease occurs gradually, Model No. 3 simulates it as a sudden drop; nonetheless, it still succeeds in capturing the overall attenuation trend (Figure 42a).

For Cell P6, all three models predict the pore pressure in a relatively consistent manner. Although the predictions are similar, Model No. 3 offers a more accurate representation of pore pressure compared to Models No. 1 and 2 (Figure 42 b). After day 380, Model No. 3 aligns more closely with the measurements than either Model No. 1 or Model No. 2.

For Cell P10, Model No. 3 shows better agreement with the measurements compared to Models No. 1 and 2 (Figure 42c). Although all three models exhibit a deviation from the measured pore pressure starting from the onset of dam impoundment (day 0), Model No. 3 consistently demonstrates a smaller deviation between the calculated and measured values throughout the period (Figure 42c). However, at day 442, the pore pressure increases, a trend that none of the models is able to predict.
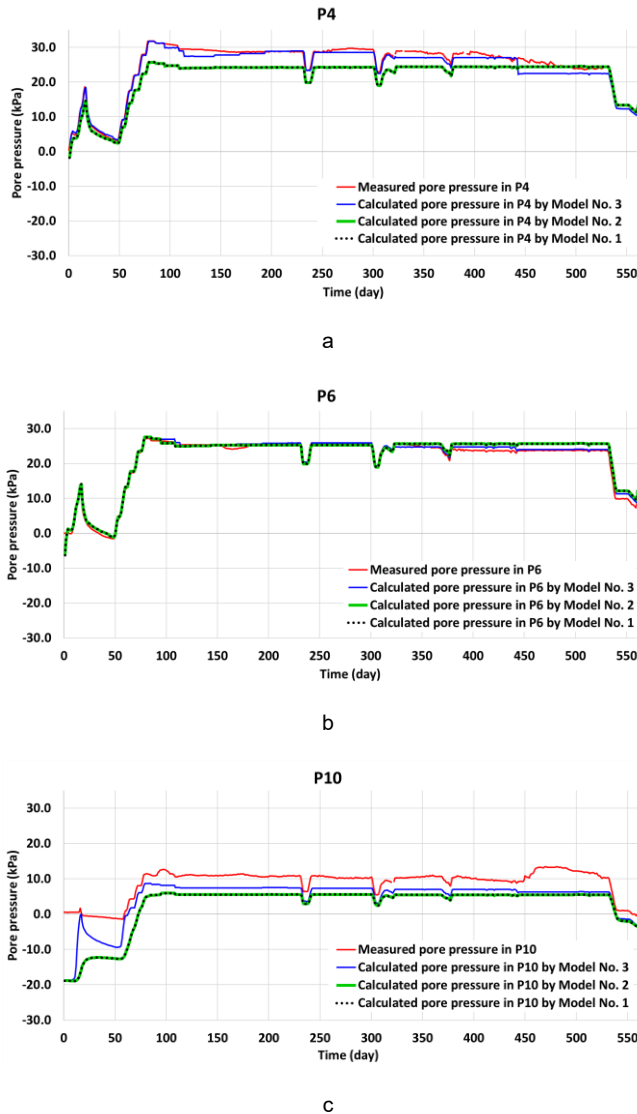

Figure 42. The measured pore pressure by Cells P4, P6 and P10 and the calculated pore pressures by the seepage models in; a) P4, b) P6 and c) P10.

5.6 Methodological strengths and limitations

The results of this study demonstrate that ERT can successfully detect internal erosion processes and related defects within the dam core. Several of the intentionally introduced defects were clearly imaged in the resistivity models, and anomalies identified through ERT were later confirmed by direct observations following dam removal. This highlights the method's capacity to provide warnings of spatially localized weaknesses. IP measurements further supported these findings, detecting several of the same zones affected by internal erosion, although less distinctly than ERT. Nevertheless, regions with high resistivity anomalies often coincided with zones of reduced chargeability, indicating pore-space changes consistent with erosion. The complementary information provided by the two methods strengthens the overall interpretation.

At the same time, the study revealed important methodological challenges that should be acknowledged. Detection capability is strongly dependent on electrode coverage and data density. Limited electrode access in peripheral zones of the dam, particularly near the abutments, reduced resolution and introduced uncertainty in those regions.

A further limitation relates to the temporal evolution of internal erosion. While some defects were imaged early in the monitoring program, others only became detectable after several years, once erosion had progressed sufficiently to produce measurable geophysical contrasts. This suggests that the geophysical signatures of internal erosion may evolve slowly and may remain below detection thresholds in the early stages. Consequently, the methods are most powerful when implemented as part of long-term monitoring strategies rather than as one-time surveys.

Overall, the methodological strengths of this study lie in the combined use of ERT and IP, the dense multi-array data acquisition, and the 3D inversion framework, which together enabled the detection and characterization of internal erosion features. The limitations identified—data coverage loss at the dam periphery, and delayed detectability of some processes—represent challenges that can be mitigated by optimized survey design, continued long-term monitoring, and integration with complementary data sources.

The seepage model guided by ERT successfully captures most of the behaviour of the leakage rate and pore water pressure, demonstrating that this approach can enhance FE seepage modelling. Nevertheless, the model exhibits certain deviations from the observed data. These discrepancies may stem from field conditions not fully represented in the modelling assumptions, such as unaccounted variability in hydraulic conductivity, material segregation, or evolving flow paths caused by progressive internal erosion or clogging.

6 Conclusion

This thesis focused on the application and development of geoelectrical monitoring techniques—primarily 3D ERT and IP—for the detection of internal erosion and defects in embankment dams. The work was carried out in the context of a test dam constructed in Älvkarleby, Sweden, where engineered defects were embedded in the dam core and filter zones to simulate real-world damage scenarios.

The results demonstrate that geoelectrical methods, when applied using appropriate inversion models and integrated with seepage modelling, offer substantial value for dam safety monitoring:

ERT successfully identified key internal defects resembling internal erosion processes, particularly those involving coarse materials such as crushed rock zones, which are often associated with internal erosion. The effectiveness of detection, however, was strongly influenced by the resistivity contrast between the defects and the surrounding dam materials. In areas with limited data coverage, the reliability of defect detection was noticeably reduced. IP data provided complementary support to the ERT results, although it could not detect the defects as clearly and distinctly as ERT.

Structural constraints applied during the inversion of synthetic data proved to be essential. Incorporating the known dam geometry and material-specific resistivity bounds significantly enhanced the accuracy and realism of the resulting 3D models. In the absence of these constraints, the inversion results were often ambiguous and more susceptible to artifacts.

The integration of geophysical data with seepage modelling provided essential contextual insights for interpreting subsurface changes. A key contribution of this research lies in how geophysical data enhanced the material characterization within the seepage models. Specifically, resistivity-based zonation improved the representation of hydraulic conductivity and dam zonation, resulting in more accurate simulations of water movement through the dam body. This integrated approach enabled the identification of preferential flow paths and potential leakage zones, significantly advancing the predictive capability and reliability of dam safety assessments.

Time-lapse monitoring proved valuable. Long-term measurements revealed evolving anomalies, some of which corresponded with previously hidden defects.

In particular, the delayed visibility of one core defect and the detection of a fine-filter anomaly after two years highlight the importance of continuous monitoring.

A multi-method approach is essential for comprehensive dam diagnostics. This study confirmed that ERT alone can provide valuable insights; however, combining ERT with IP and numerical seepage modelling yields a more robust and reliable understanding of internal processes.

Overall, the thesis contributes a validated framework for integrating advanced geoelectrical monitoring into dam safety programs. The research highlights both the potential and the limitations of these techniques: while ERT and IP offer unique insights into the dam's internal condition, their effectiveness depends on contrast, scale, and data coverage.

7 Future research

The research presented in this thesis demonstrates the potential of geoelectrical monitoring methods, particularly 3D ERT and IP, in combination with seepage modelling, for advancing dam safety assessments. At the same time, it also highlights several areas where further investigation is needed to improve methodology, reliability, and long-term applicability.

1. Improved inversion strategies and computational techniques

Although structural constraints and resistivity bounds were found to significantly improve model accuracy, challenges remain regarding limited data coverage and the non-uniqueness of inversion results. Future research should therefore focus on more advanced approaches, including joint inversion of ERT and IP data, machine learning–based inversion strategies, and integrated modelling that combines ERT, IP, temperature, and seepage processes.

2. Enhanced integration with hydro-mechanical models

This work demonstrated the benefits of coupling geophysical and seepage models. Future studies should extend this integration to fully coupled hydro-mechanical models that simulate internal erosion processes, progressive clogging, or crack development. Such models could provide a more comprehensive understanding of dam behaviour under changing hydraulic conditions and allow for predictive simulations under different loading scenarios.

3. Long-term monitoring and automation

The time-lapse approach revealed evolving anomalies, underscoring the value of continuous monitoring. Future research should investigate automated acquisition systems capable of operating over long periods with minimal maintenance, as well as data-processing workflows that incorporate real-time anomaly detection. The development of robust monitoring networks with wireless data transmission and remote control would greatly enhance the practical implementation of geoelectrical methods in dam safety programs.

4. Field validation and scaling

The test dam in Älvkarleby provided a unique opportunity to validate methods under controlled conditions. Future research should focus on scaling these approaches to large, operational dams with more complex geometries, heterogeneous materials,

and varying hydrological regimes. Comparative studies across different dam types and climates would strengthen the generalizability of the findings.

8 References

Abdulsamad, F., Revil, A., Soueid Ahmed, A., Coperey, A., Karaoulis, M., Nicaise, S., & Peyras, L. (2019). Induced polarization tomography applied to the detection and the monitoring of leaks in embankments. *Engineering Geology*, *254*, 89–101. https://doi.org/10.1016/j.enggeo.2019.04.001

Adamo, N., Al-Ansari, N., Sissakian, V., Laue, J., & Knutsson, S. (2020). Dam Safety Problems Related to Seepage. *Journal of Earth Sciences and Geotechnical Engineering*, *10*(6), 191–239. https://www.scienpress.com/journal_focus.asp?main_id=59&Sub_id=IV&Issue=1853855https://www.scienpress.com/journal_focus.asp?main_id=59&Sub_id=IV&Issue=1853855

Archie, G. E. (1942). The Electrical Resistivity Log as an Aid in Determining Some Reservoir Characteristics. *Transactions of the AIME*, *146*(01), 54–62. https://doi.org/10.2118/942054-G

Bayat, M., Eslamian, S., Shams, G., & Hajiannia, A. (2019). The 3D analysis and estimation of transient seepage in earth dams through PLAXIS 3D software: neural network. *Environmental Earth Sciences*, *78*(18), 571. https://doi.org/10.1007/s12665-019-8405-y

Bernstone, C., Lagerlund, J., Toromanovic, J., & Juhlin, C. (2021). *Deformationer och portryck i en experimentell fyllningsdamm*. Energiforsk. https://energiforsk.se/program/dammsakerhet/rapporter/deformationer-och-portryck-i-en-experimentell-fyllningsdamm-2021-772/

Bièvre, G., Oxarango, L., Günther, T., Goutaland, D., & Massardi, M. (2018). Improvement of 2D ERT measurements conducted along a small earth-filled dyke using 3D topographic data and 3D computation of geometric factors. *Journal of Applied Geophysics*, *153*, 100–112. https://doi.org/10.1016/j.jappgeo.2018.04.012

Bing, Z., & Greenhalgh, S. A. (2000). Cross-hole resistivity tomography using different electrode configurations. *Geophysical Prospecting*, *48*(5), 887–912. https://doi.org/10.1046/j.1365-2478.2000.00220.x

Binley, A., & Slater, L. (2020). *Resistivity and Induced Polarization: Theory and Applications to the Near-Surface Earth*. Cambridge University Press. https://doi.org/DOI: 10.1017/9781108685955

Bonelli, S., & Nicot, F. (Eds.). (2013). *Erosion in Geomechanics Applied to Dams and Levees*. Wiley. https://doi.org/10.1002/9781118577165

Brebbia, C. A. (1984). The boundary element method in engineering practice. *Engineering Analysis*, *1*(1), 3–12. https://doi.org/10.1016/0264-682X(84)90004-2

Brown, A. J., & Gosden, J. D. (2004). *Interim Guide to Quantitative Risk Assessment for UK Reservoirs*. Thomas Telford.

Cheng, Q., Chen, X., Tao, M., & Binley, A. (2019). Characterization of karst structures using quasi-3D electrical resistivity tomography. *Environmental Earth Sciences*, *78*(9), 285. https://doi.org/10.1007/s12665-019-8284-2

Chi, F., Breul, P., Carvajal, C., & Peyras, L. (2023). Stochastic seepage analysis in embankment dams using different types of random fields. *Computers and Geotechnics*, *162*. https://doi.org/10.1016/j.compgeo.2023.105689

Cho, I., Ha, I., Kim, K., Ahn, H., Lee, S., & Kang, H. (2014). 3D effects on 2D resistivity monitoring in earth-fill dams. *Near Surface Geophysics*, *12*(1), 73–81. https://doi.org/10.3997/1873-0604.2013065

Dahlin, T., & Zhou, B. (2006). Multiple-gradient array measurements for multichannel 2D resistivity imaging. *Near Surface Geophysics*, *4*(2), 113–123. https://doi.org/10.3997/1873-0604.2005037

Daily, W., Ramirez, A., LaBrecque, D., & Nitao, J. (1992). Electrical resistivity tomography of vadose water movement. *Water Resources Research*, *28*(5), 1429–1442. https://doi.org/10.1029/91WR03087

Dey, A., & Morrison, H. F. (1979). Resistivity modeling for arbitrarily shaped three-dimensional structures. *Geophysics*, *44*, 753–780. https://api.semanticscholar.org/CorpusID:121902845

EL-Molla, D. A., & Kilit, M. (2025). Seepage Control, Detection, and Treatment in Embankment Dams: A State-of-the-Art Review. *Arabian Journal for Science and Engineering*. https://doi.org/10.1007/s13369-025-10185-y

Fannin, R. J., & Slangen, P. (2014). On the distinct phenomena of suffusion and suffosion. *Géotechnique Letters*, *4*(4), 289–294. https://doi.org/10.1680/geolett.14.00051

Fargier, Y., Lopes, S. P., Fauchard, C., François, D., & Côte, P. (2014). DC-Electrical Resistivity Imaging for embankment dike investigation: A 3D extended normalisation approach. *Journal of Applied Geophysics*, *103*, 245–256. https://doi.org/10.1016/j.jappgeo.2014.02.007

Federico, F. (2017). Particle Migration Phenomena Related to Hydromechanical Effects at Contact between Different Materials in Embankment Dams. In *Granular Materials*. InTech. https://doi.org/10.5772/67785

Fell, R., & Fry, J.-J. (2007). *Internal Erosion of Dams and Their Foundations*. CRC Press. https://doi.org/10.1201/9781482266146

Fell, R., MacGregor, P., Stapledon, D., Bell, G., & Foster, M. (2014). *Geotechnical Engineering of Dams (2nd ed.)*. CRC Press. https://doi.org/https://doi.org/10.1201/b17800

Fell, R., Wan, C. F., Cyganiewicz, J., & Foster, M. (2003). Time for Development of Internal Erosion and Piping in Embankment Dams. *Journal of Geotechnical*

and Geoenvironmental Engineering, *129*(4), 307–314. https://doi.org/10.1061/(ASCE)1090-0241(2003)129:4(307)

Foster, M., Fell, R., & Spannagle, M. (1998). *Analysis of embankment dam incidents / M.A. Foster, R. Fell and M. Spannagle*. University of New South Wales. School of Civil and Environmental Engineering.

Foster, M., Fell, R., & Spannagle, M. (2000). The statistics of embankment dam failures and accidents. *Canadian Geotechnical Journal*, *37*(5), 1000–1024. https://doi.org/https://doi.org/10.1139/t00-030

Fry, J. J. (2016). Lessons on internal erosion in embankment dams from failures and physical models. *Proc., 8th Int. Conf. on Scour and Erosion (ICSE8)*, 41–58.

Gabbouj, M., Coyle, E. J., & Gallagher, N. C. (1992). An overview of median and stack filtering. *Circuits, Systems and Signal Processing*, *11*(1), 7–45. https://doi.org/10.1007/BF01189220

Guo, Y., Cui, Y., Xie, J., Luo, Y., Zhang, P., Liu, H., & Liu, J. (2022). Seepage detection in earth-filled dam from self-potential and electrical resistivity tomography. *Engineering Geology*, *306*, 106750. https://doi.org/10.1016/j.enggeo.2022.106750

Hansson, N., Helgesson, A., & Lagerlund, J. (2024). *Embankment Test Dam of Älvkarleby – Data from seepage and turbidity measurements*. Mendeley Data, V3. https://doi.org/10.17632/zhfx2g7s7b.3

Hojat, A., Ferrario, M., Arosio, D., Brunero, M., Ivanov, V. I., Longoni, L., Madaschi, A., Papini, M., Tresoldi, G., & Zanzi, L. (2021). Laboratory Studies Using Electrical Resistivity Tomography and Fiber Optic Techniques to Detect Seepage Zones in River Embankments. *Geosciences*, *11*(2), 69. https://doi.org/10.3390/geosciences11020069

ICOLD. (1973). *Lessons from dam incidents* (2nd ed.). International Commission on Large Dams. Committee on Failures and Accidents to Large Dams. https://books.google.se/books?id=OPXgoQEACAAJ

ICOLD. (1983). *Deterioration of dams and reservoirs, examples and their analysis*. International Commission on Large Dams. Committee on Deterioration of Dams and Reservoirs. https://books.google.se/books?id=k8BonQAACAAJ

ICOLD. (1994). *Embankment dams: granular filters and drains. Review and recommendations: Vol. Bulletin 95*. International Commission on Large Dams.

ICOLD. (1995). *Dam failures statistical analysis: Vol. Bulletin 99*. International Commission on Large Dams. Committee on Dam Safety.

ICOLD. (2014). *Dam surveillance guide: Vol. Bulletin 158*. International Commission on Large Dams.

Ingeman-Nielsen, T., Tomaškovičová, S., & Dahlin, T. (2016). Effect of electrode shape on grounding resistances — Part 1: The focus-one protocol. *GEOPHYSICS*, *81*(1), WA159–WA167. https://doi.org/10.1190/geo2015-0484.1

Interagency Committee on Dam Safety (ICODS). (2015). *Evaluation and monitoring of seepage and internal erosion (FEMA P-1032)*. Washington, D.C. : Federal Emergency Management Agency.

Johnson, T. C., Versteeg, R. J., Ward, A., Day-Lewis, F. D., & Revil, A. (2010). Improved hydrogeophysical characterization and monitoring through parallel modeling and inversion of time-domain resistivity andinduced-polarization data. *GEOPHYSICS*, *75*(4), WA27–WA41. https://doi.org/10.1190/1.3475513

Jung, I.-S., Berges, M., Garrett, J. H., & Poczos, B. (2015). Exploration and evaluation of AR, MPCA and KL anomaly detection techniques to embankment dam piezometer data. *Advanced Engineering Informatics*, *29*(4), 902–917. https://doi.org/https://doi.org/10.1016/j.aei.2015.10.002

Karaoulis, M. C., Kim, J.-H., & Tsourlos, P. I. (2011). 4D active time constrained resistivity inversion. *Journal of Applied Geophysics*, *73*(1), 25–34. https://doi.org/10.1016/j.jappgeo.2010.11.002

Khalil, M. A., Barrick, D., & Joeckel, R. M. (2024). Characterization of seepage in an earthfill dam by the integration of geophysical surveys and geotechnical data. *Journal of Applied Geophysics*, *220*, 105273. https://doi.org/10.1016/j.jappgeo.2023.105273

Knödel, K., Lange, G., & Voigt, H.-J. (2007). *Environmental Geology*. Springer Berlin Heidelberg. https://doi.org/10.1007/978-3-540-74671-3

LaBrecque, D. J., & Yang, X. (2001). Difference Inversion of ERT Data: a Fast Inversion Method for 3-D In Situ Monitoring. *Journal of Environmental and Engineering Geophysics*, *6*(2), 83–89. https://doi.org/10.4133/JEEG6.2.83

Lagerlund, J. (2025). *Documentation from the dismantling of the Älvkarleby test embankment dam*. Energiforsk.

Lagerlund, J., Bernstone, C., Viklander, P., & Nordström, E. (2022). Embankment Test Dam of Älvkarleby - Description of installed defects and their position. In *Mendeley Data*. Mendeley Data, V3. https://doi.org/10.17632/k7zrrbxxnb.3

Lee, B., Oh, S., & Yi, M.-J. (2020). Mapping of leakage paths in damaged embankment using modified resistivity array method. *Engineering Geology*, *266*, 105469. https://doi.org/10.1016/j.enggeo.2019.105469

Loke, M. H. (2002). *Tutorial : 2-D and 3-D electrical imaging surveys*. www.geoelectrical.com

Marshall, D. J., & Madden, T. R. (1959). INDUCED POLARIZATION, A STUDY OF ITS CAUSES. *GEOPHYSICS*, *24*(4), 790–816. https://doi.org/10.1190/1.1438659

Martínez-Moreno, F. J., Delgado-Ramos, F., Galindo-Zaldívar, J., Martín-Rosales, W., López-Chicano, M., & González-Castillo, L. (2018). Identification of leakage and potential areas for internal erosion combining ERT and IP techniques at the Negratín Dam left abutment (Granada, southern Spain). *Engineering Geology*, *240*, 74–80. https://doi.org/10.1016/j.enggeo.2018.04.012

Masi, M., Ferdos, F., Losito, G., & Solari, L. (2020). Monitoring of internal erosion processes by time-lapse electrical resistivity tomography. *Journal of Hydrology*, *589*, 125340. https://doi.org/10.1016/j.jhydrol.2020.125340

Nikrou, P., & Pirboudaghi, S. (2024). Seepage analysis and control of the Sahand rockfill dam drainage using instrumental data. *ArXiv*, *abs/2410.06079*. https://api.semanticscholar.org/CorpusID:273227951

Norooz, R., Nivorlis, A., Olsson, P.-I., Günther, T., Bernstone, C., & Dahlin, T. (2024). Monitoring of Älvkarleby test embankment dam using 3D electrical resistivity tomography for detection of internal defects. *Journal of Civil Structural Health Monitoring*, *14*(5), 1275–1294. https://doi.org/10.1007/s13349-024-00785-x

Norooz, R., Olsson, P.-I., Dahlin, T., Günther, T., & Bernstone, C. (2021). A geoelectrical pre-study of Älvkarleby test embankment dam: 3D forward modelling and effects of structural constraints on the 3D inversion model of zoned embankment dams. *Journal of Applied Geophysics*, *191*, 104355. https://doi.org/10.1016/j.jappgeo.2021.104355

Novak, P., Moffat, I., Nalluri, C., & Narayanan, R. (2014). *Hydraulic Structures* (Fourth Edition). CRC Press. https://doi.org/10.1201/9781315274898

Olsson, P.-I., Fiandaca, G., Larsen, J. J., Dahlin, T., & Auken, E. (2016). Doubling the spectrum of time-domain induced polarization by harmonic de-noising, drift correction, spike removal, tapered gating and data uncertainty estimation. *Geophysical Journal International*, *207*(2), 774–784. https://doi.org/10.1093/gji/ggw260

Penman, A. D. M. (1986). On the embankment dam. *Géotechnique*, *36*(3), 303–348. https://doi.org/10.1680/geot.1986.36.3.303

Regan, P. J. (2009). An Examination of Dam Failures vs. Age of Dams. *U.S. Society on Dams, Denver, Colorado*.

Revil, A., Vaudelet, P., Su, Z., & Chen, R. (2022). Induced Polarization as a Tool to Assess Mineral Deposits: A Review. *Minerals*, *12*(5), 571. https://doi.org/10.3390/min12050571

Richards, K. S., & Reddy, K. R. (2007). Critical appraisal of piping phenomena in earth dams. *Bulletin of Engineering Geology and the Environment*, *66*(4), 381–402. https://doi.org/10.1007/s10064-007-0095-0

Richardson, L. F. (2007). *Weather Prediction by Numerical Process*. Cambridge University Press. https://books.google.se/books?id=D52d3_bbgg8C

Rink, M. ; S. J. R. (1974, June). Interface Conductivity And Its Implications To Electric Logging. *SPWLA 15th Annual Logging Symposium.*

Robbins, B. A., & Griffiths, D. V. (2018). Internal Erosion of Embankments: A Review and Appraisal. *Rocky Mountain Geo-Conference 2018*, 61–75. https://doi.org/10.1061/9780784481936.005

Rönnqvist, H., & Viklander, P. (2016). A unified-plot approach for the assessment of internal erosion in embankment dams. *International Journal of*

Geotechnical Engineering, *10*(1), 66–80. https://doi.org/10.1179/1939787915Y.0000000002

Rücker, C., & Günther, T. (2011). The simulation of finite ERT electrodes using the complete electrode model. *GEOPHYSICS*, *76*(4), F227–F238. https://doi.org/10.1190/1.3581356

Rücker, C., Günther, T., & Wagner, F. M. (2017). pyGIMLi: An open-source library for modelling and inversion in geophysics. *Computers & Geosciences*, *109*, 106–123. https://doi.org/https://doi.org/10.1016/j.cageo.2017.07.011

Sasaki, Y. (1994). 3-D resistivity inversion using the finite-element method. *GEOPHYSICS*, *59*(12), 1839–1848. https://doi.org/10.1190/1.1443571

Shin, S., Park, S., & Kim, J.-H. (2019). Time-lapse electrical resistivity tomography characterization for piping detection in earthen dam model of a sandbox. *Journal of Applied Geophysics*, *170*, 103834. https://doi.org/10.1016/j.jappgeo.2019.103834

Si, H. (2015). TetGen, a Delaunay-Based Quality Tetrahedral Mesh Generator. *ACM Transactions on Mathematical Software*, *41*(2), 1–36. https://doi.org/10.1145/2629697

Sjödahl, P. (2006). *Resistivity investigation and monitoring for detection of internal erosion and anomalous seepage in embankment dams* [Doctoral Thesis, Lund University]. https://portal.research.lu.se/en/publications/resistivity-investigation-and-monitoring-for-detection-of-interna

Sjödahl, P., Dahlin, T., & Johansson, S. (2005). Using resistivity measurements for dam safety evaluation at Enemossen tailings dam in southern Sweden. *Environmental Geology*, *49*(2), 267–273. https://doi.org/10.1007/s00254-005-0084-1

Sjödahl, P., Dahlin, T., & Johansson, S. (2010). Using the resistivity method for leakage detection in a blind test at the Røssvatn embankment dam test facility in Norway. *Bulletin of Engineering Geology and the Environment*, *69*(4), 643–658. https://doi.org/10.1007/s10064-010-0314-y

Sjödahl, P., Dahlin, T., Johansson, S., & Loke, M. H. (2008). Resistivity monitoring for leakage and internal erosion detection at Hällby embankment dam. *Journal of Applied Geophysics*, *65*(3), 155–164. https://doi.org/https://doi.org/10.1016/j.jappgeo.2008.07.003

Smith, G. D. (1985). *Numerical Solution of Partial Differential Equations: Finite Difference Methods*. Oxford: Clarendon Press. https://books.google.se/books?id=hDpvljaHOrMC

Tejero-Andrade, A., Cifuentes, G., Chávez, R. E., López-González, A. E., & Delgado-Solórzano, C. (2015). L- and CORNER-arrays for 3D electric resistivity tomography: an alternative for geophysical surveys in urban zones. *Near Surface Geophysics*, *13*(4), 355–368. https://doi.org/10.3997/1873-0604.2015015

Tikhonov, A. N., & Arsenin, V. I. (Vasiliĭ I. (1977). Solutions of ill-posed problems. In *Scripta series in mathematics*. Winston,distributed solely by Halsted Press. https://cir.nii.ac.jp/crid/1130000795395932288

Toromanovic, J. (2024). *Monitoring and Modelling of Embankment Dams* [Doctoral thesis, Luleå University of Technology]. https://ltu.diva-portal.org/smash/record.jsf?pid=diva2%3A1847703&dswid=-7138

Udphuay, S., Günther, T., Everett, M. E., Warden, R. R., & Briaud, J.-L. (2011). Three-dimensional resistivity tomography in extreme coastal terrain amidst dense cultural signals: application to cliff stability assessment at the historic D-Day site. *Geophysical Journal International*, *185*(1), 201–220. https://doi.org/10.1111/j.1365-246X.2010.04915.x

US Bureau of Reclamation. (2012). *Embankment Dams, Design Standards No. 13: Vol. DS-13(2)-10* (Phase 4 (Final)).

USACE. (2012). *Mississippi River and Tributaries System 2011 post-flood report: Documenting the 2011 Flood, the Corps' response, and the performance of the MR&T System* (H. DeHaan, J. Stamper, & B. Walters, Eds.).

Waxman, M. H., & Smits, L. J. M. (1968). Electrical Conductivities in Oil-Bearing Shaly Sands. *Society of Petroleum Engineers Journal*, *8*(02), 107–122. https://doi.org/10.2118/1863-A

Wei, Y., Shi, Z., Wang, C., & Huang, M. (2024). Joint imaging of ERT datasets and its application in seepage characterization at Nanshan Dam, southeast China. *Journal of Applied Geophysics*, *225*, 105390. https://doi.org/10.1016/j.jappgeo.2024.105390

Zheng, X., Yan, B., Wang, W., Du, K., & Fang, Y. (2024). Seepage–Deformation Coupling Analysis of a Core Wall Rockfill Dam Subject to Rapid Fluctuations in the Reservoir Water Level. *Water*, *16*(11), 1621. https://doi.org/10.3390/w16111621

Zhou, B., Bouzidi, Y., Ullah, S., & Asim, M. (2020). A full-range gradient survey for 2D electrical resistivity tomography. *Near Surface Geophysics*, *18*(6), 609–626. https://doi.org/10.1002/nsg.12125

$$\nabla \cdot (\sigma \nabla \varphi) = -I\delta(r - r_s)$$

$$K = 2\pi \left(\frac{1}{AM} - \frac{1}{BM} - \frac{1}{AN} + \frac{1}{BN} \right)^{-1}$$

$$\frac{\partial}{\partial x}\left(-k_x \frac{\partial h}{\partial x}\right) + \frac{\partial}{\partial y}\left(-k_y \frac{\partial h}{\partial y}\right) + \frac{\partial}{\partial z}\left(-k_z \frac{\partial h}{\partial z}\right) = \frac{\partial \theta}{\partial t}$$

$$\sigma_{el} = \frac{1}{F}\sigma_w$$

$$Reciprocal\ error_{resistivity} = \left| \frac{R_1 - R_2}{(R_1 + R_2)/2} \right| \times 100$$

$$\rho_a = K \cdot \frac{\Delta V}{I}$$

$$Reciprocal\ error_{IP} = |M_1 - M_2|$$

$$m_t = \frac{1}{V_{DC}} \int_{t_1}^{t_2} V_s(t)dt$$

$$d_{calc} = F(m)$$

$$\sigma = \sigma_{el} + \sigma_{surf}$$

$$y_i^{backward} = \frac{y_{i-1} + f x_i}{1 + f}$$

$$\sigma'' = \sigma''_{surf}$$

$$J_k^T W_d^T W_d J_k \Delta m_k = J_k^T W_d^T W_d (d_{obs} - F(m_k))$$

$$\nabla \cdot (\sigma \nabla \varphi) = -I\delta(r - r_s)$$

$$y_i^{backward} = clip(y_i^{backward}, y_{i-1} - max_{impact}.|y_{i-1}|, y_{i-1} + max_{impact}.|y_{i-1}|)$$

$$\sigma^* = \sigma' + i\sigma''$$

$$\sigma = \frac{1}{F}\sigma_w + \sigma_{surf}$$

LUND UNIVERSITY

Division of Engineering Geology
Department of Biomedical Engineering
Faculty of Engineering